Fracture Initiation near a Circular Cavity

A THESIS
SUBMITTED TO THE FACULTY OF THE GRADUATE SCHOOL
OF THE UNIVERSITY OF MINNESOTA
BY

Derrick Blanksma

IN PARTIAL FULFILLMENT OF THE REQUIREMENTS
FOR THE DEGREE OF
MASTER OF SCIENCE

Professor Joseph F. Labuz

May 2013

Abstract

Initiation of fracture from a circular cavity was monitored with a cavity expansion apparatus for two rock materials: Berea sandstone and Indiana limestone. Fracture characteristic from cavity expansion tests were compared to three-point-bending (3PB) tests on the same rock.

Using a particle tracking technique called digital image correlation (DIC), a discontinuity in the displacement field near the cavity boundary was identified at 80% and 60% peak internal pressure for Berea sandstone and Indiana limestone, respectively. The critical crack opening displacement (CCOD) was assumed to be associated with unstable crack growth from the 3PB tests, which occurs at peak loading. The CCOD measurements from three-point-bend tests were 51-58μm for Berea sandstone and 15-16μm for Indiana limestone. The measured COD from the cavity expansion test at peak pressure was 57-90μm for Berea sandstone and 20-24μm for Indiana limestone. The results show the CCOD from cavity expansion were on average 35% higher than three-point-bend test for Berea sandstone and 40% higher for Indiana limestone, suggesting stable growth prior to peak pressure.

Table of Contents

List of Tables

List of Figures

Chapter 1

Introduction

An experiment is a question which science poses to Nature and a measurement is a recording of Nature's answer.

~ Max Planck (1858-1947)

1.1 Motivation

The analysis of fracture near a cavity in rock has been largely motivated by the extraction of petroleum and natural gas from a borehole. Stimulation of oil production by pressurizing a portion of a borehole was first used by the oil industry in the 1940's. Since then a great amount of work has been focused on fracture from a borehole. Today, novel methods for fracturing boreholes in rock are being developed to promote safety and economic reliability. By better understanding the initiation of a fracture from a circular cavity these ambitions can be met.

The problem of an expanding circular cavity in a mass is often considered one of the most important problems in rock mechanics (Jaeger & Cook, 1969). Tunnels, production wells, and cavities in rock are all governed by this problem. Elastic analysis of these structures often breaks down when inhomogeneity's, such as a fracture is introduced into the mass. However, small-scale ($10^{-3} – 10^{-6}$ *m*) analysis may provide a better understanding of the initiation of a fracture from a circular cavity. This thesis explores the small-scale details of the development of a fracture near an expanding circular cavity.

1.2 Objective

The objectives of this work are to

1) develop a novel apparatus to monitor cavity expansion;

2) investigate how a fracture initiates near a circular cavity subjected to various stress distributions;

3) use digital image correlation to investigate crack opening displacements;

4) analyze and describe events associated with the initiation of fracture;

1.3 Scope and Organization

Chapter 2 reviews the fundamentals of linear fracture mechanics and the problem of a fracture near a circular cavity. Chapter 2 also gives a brief description of the digital image correlation (DIC) technique used for measuring the displacement field.

Chapter 3 begins by presenting different loading distributions to induce fracture. Three different distributions of stress in a circular cavity are presented in the context of linear elasticity to highlight how fracture was produced.

Chapter 3 continues with a detailed description of the loading apparatus as well as the device used to pressurize the cavity, commonly called a “packer”. The design of the packer is highlighted in as well as the method used to calibrate the packer. Chapter 3 finishes with a description of the different kinds of rock tested as well as the experimental procedure.

Chapter 4 highlights the results of experiments. Elastic analysis of the shear modulus from DIC measurement is presented for each type of rock. Also, fracture characteristics are compared with other experiments. Chapter 5 concludes with comments on the outcomes of the experiments and remarks on future developments.

Chapter 2

Background

2.1 Linear Fracture Mechanics

Some of the first developments in fracture mechanics were by English engineers C.E. Inglis (1913) and A.A. Griffith (1920). Inglis' work focused on providing a mathematical formalism for the stress concentration around an elliptical hole in a solid. Griffith, aware of this work, later considered how the Inglis solution might predict fracture for a material containing a crack. However, according to the Inglis solution for a perfectly sharp crack, the stresses would approach infinity at the crack tip and consequently the material would have *zero* strength. Instead of focusing on stresses at the crack tip, Griffith developed the concept of fracture based on an energy-balance approach. Griffith's energy criterion states that crack growth will occur when the strain energy released by a virtual extension of the crack equals the energy absorbed by the material in that crack advance (Griffith, 1920). Griffith showed that the strain energy per unit thickness, U, due to the presence of a crack of length $2a$, in an infinite plate subjected to uniform tension, σ, is

$$U = -\frac{\pi\sigma^2 a^2}{E'} \tag{1}$$

E' = Young's modulus (E) for plane stress and $E' = E/(1-\nu^2)$ for plane strain. The negative sign indicates energy is released from the system by crack growth. The surface energy S associated with the creation of a traction free crack of length $2a$ (and unit thickness) is

$$S = 4\gamma a \tag{2}$$

where γ is the surface energy [Joules/meter^2].

The strain energy released when the crack grows by an amount *da* is

$$\frac{\partial(S+U)}{\partial a} = 4\gamma - \frac{2\pi\sigma^2 a}{E'} \tag{3}$$

The value of the critical crack length, a_c is found by setting (3) to zero. When this condition is satisfied, crack growth is imminent. The stress at the critical condition is

$$\sigma_c = \sqrt{\frac{2E'\gamma}{\pi a_c}} \tag{4}$$

Griffith's criterion was developed from fracture observations on a brittle material, specifically glass. It was later realized by Irwin (1948) and Orowan (1949) that when ductile materials are considered, a vast majority of the strain energy released is not in the creation of new surface but rather in the formation of a non-linear plastic zone at the crack tip. A general expression for the *critical strain energy release rate*, G_c is

$$G_c = \frac{\sigma_c^2 \pi a_c}{E'} \tag{5}$$

where G_c accounts for *all* the strain energy "sinks" that contribute to fracture.

Irwin (1958) developed the concept of the stress intensity factor, *K*, which quantifies the intensity of the stress singularity at a crack tip. Generally the formula for *K* is as follows:

$$K_i = \sigma\sqrt{\pi a} f(\alpha) \tag{6}$$

K_i is the stress intensity factor with *i=I,II,III* for mode I (opening mode), mode II (sliding mode) and mode-III (tearing mode), σ is the applied stress, a is the crack length, $f(\alpha)$ is a shape factor that depends on the geometry of the specimen and $\alpha = a/D$, where *D* is a specimen length. A crack will advance when a critical stress intensity value, K_{ic}, is reached. The critical value is often called the fracture toughness and for mode I fracture the fracture toughness is

$$K_{Ic} = \sigma_c \sqrt{\pi a} f(\alpha) \tag{7}$$

where σ_c is the critical stress.

2.2 Critical Crack Opening Displacement

If a stress-based approach is considered, then the stress close to the crack tip approaches infinity due to the inverse relationship with the distance from the crack tip, r (Figure 1).

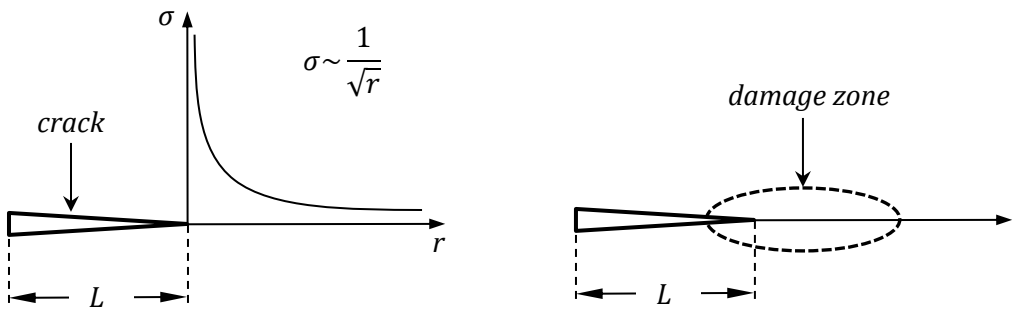

Figure 1: (Left) The inverse relationship of stress and distance from the crack tip. (Right) The development of a damage zone due to the stress singularity.

Because of the singularity, a damage zone develops at the tip and extends for some finite length and width into the medium. For brittle materials, the damage zone is characterized by a zone of progressive softening due to the formation of microcracks (Bažant & Planas, 1998).

If the condition that the damage zone is sufficiently small compared to the size of the structure, then the damaged zone can be considered as part of the *effective* crack length which consists of the crack length, L, and the length of a fracture process zone (FPZ), l_p. Furthermore, it is important to note that the FPZ is modeled by cohesive tractions along the FPZ due to ligaments that remain unbroken as the surfaces separate (Barrenblatt, 1959;

Dugdale, 1960). Ultimately, the opening displacement between the two surfaces reaches a critical value, w_c, and the traction becomes zero. Figure 2 shows a visual depiction of the model.

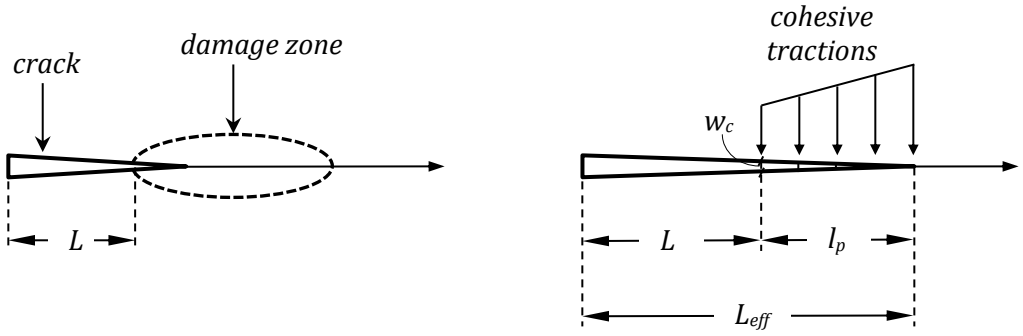

Figure 2: (Right) Damage zone developed from crack tip. (Left) Model of crack and damage zone as an effective crack length, L_{eff}.

The FPZ length was observed experimentally by Labuz and Biolzi (1998) through locations of acoustic emission (AE). Transducers, attached to a granite beam, detect acoustic emissions which are caused by the development of microcracks. At peak load, the events localize and provide an estimate for the length and width of the FPZ. Properties of the FPZ for beam specimens of Berea sandstone was also investigated three-point-bending by Lin and Labuz (2013) using a particle tracking technique based on digital image correlation (DIC).

2.3 Fracture near an Expanding Circular Cavity

Bowie (1956) and Newman (1969, 1971) presented a comprehensive analytical and numerical treatment of a fracture near a circular cavity. Among others, the problem was further developed by Beuckner (1960), Hardy (1973), Ingraffea (1977), and experimentally by Clifton *et al.* (1976).

The solution for a circular hole with radial cracks subjected to internal pressure in the cavity can be approximated by the problem of a plate with an edge notch under uniform tension (Figure 3).

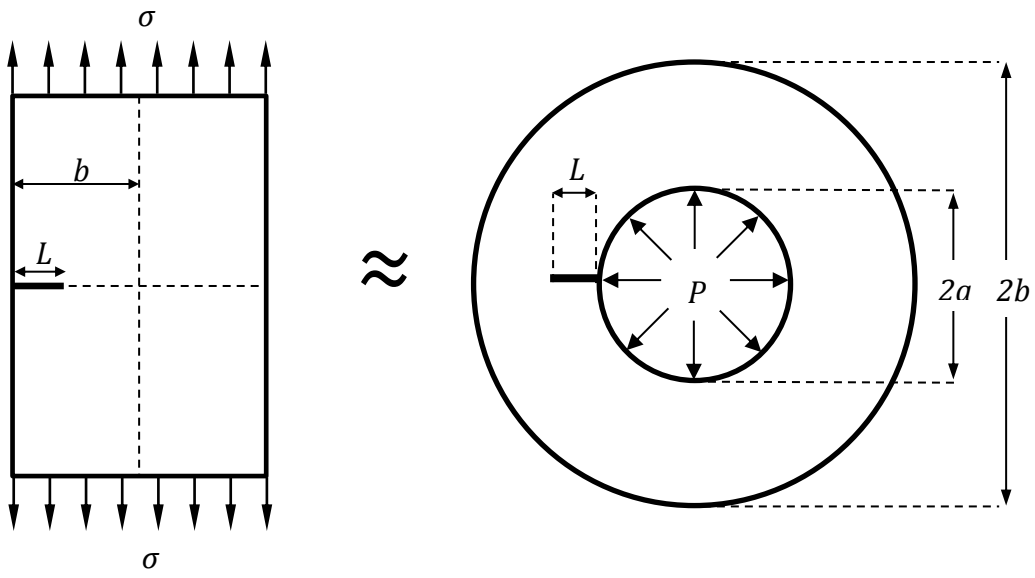

Figure 3: (Left) A rectangular plate with edge cracks and uniform tension. (Right) A hollow cylinder subjected to internal pressure with two radial cracks .

Bowie and Freese (1972) produced solutions for the stress intensity as a function of crack length for the case of one and two radial cracks (Figures 4 and 5).

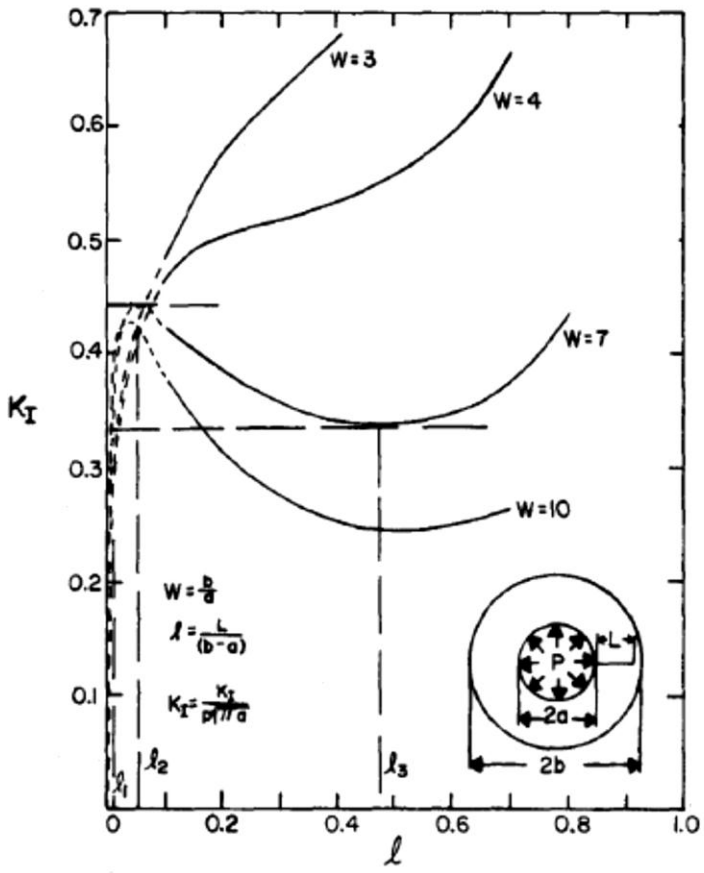

Figure 4: Stress intensity of a jacketed cylinder with one radial crack – (Bowie and Freese, 1972)

The plot in Figure 4 shows the dimensionless stress intensity, K_I^* as a function of the dimensionless length, ℓ and different values of W for a single radial crack, where

$$\ell = \frac{L}{(b-a)} \qquad\qquad W = \frac{b}{a} \tag{8}$$

The important thing to note is that for large values of W, stable crack growth can occur. For example, consider $W = 7$ in Figure 4. If $\ell_i < \ell_1$, then unstable crack growth occurs, since $\partial K_I/\partial \ell > 0$. For $\ell_1 < \ell_i < \ell_2$, unstable crack growth occurs, but the transition to *stable* crack growth occurs once $\ell_i = \ell_2$. If $\ell_2 < \ell_i < \ell_3$, then *stable* crack growth occurs, since $\partial K_I/\partial \ell < 0$. Finally, if $\ell_i > \ell_3$, then unstable crack growth occurs.

Figure 5 shows the stress intensity curves for a hollow cylinder with two diametrically opposed radial cracks.

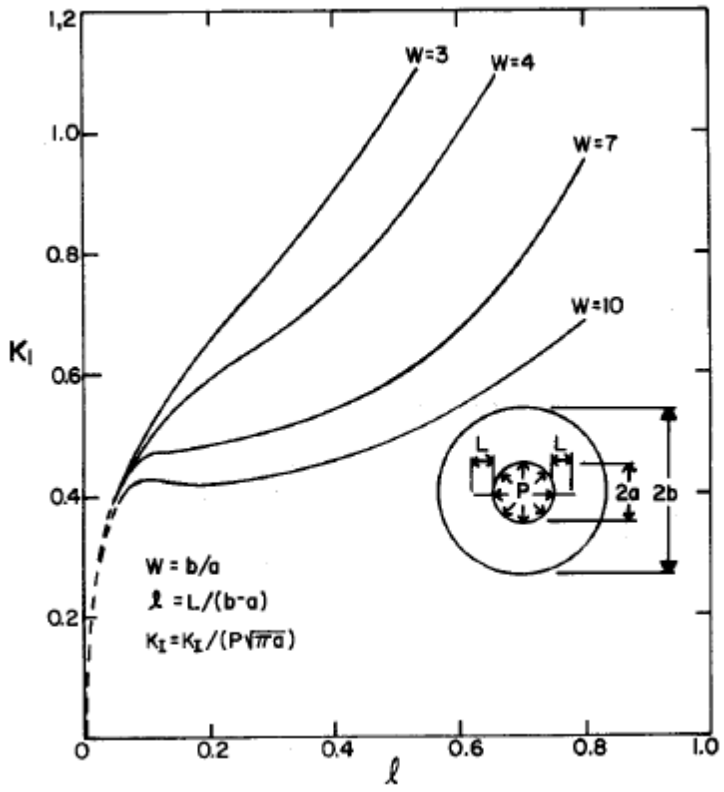

Figure 5: Stress intensity for a jackeedt cylinder with two radial cracks – (Bowie and Freese, 1972)

For the case of two radial cracks with very small crack lengths, Koiter (1965) and Bowie (1964) mutually concluded through a rigorous analysis that the stress intensity factor for this problem is:

$$K_I = CP\sqrt{L} \tag{9}$$

where C is a numerically derived constant equal to 1.1215. For larger crack lengths, the stress intensity depends on crack length and specimen geometry. It is important to note that a large value of W will promote stable crack growth.

The initiation of two cracks or one crack can be viewed as a competition between the dimensionless stress intensity factors in Figures 5 and 6. If K_I* is evaluated at the same

crack length ℓ for the same W, then whichever dimensionless stress intensity is larger, or the pressure is smaller, will indicate the formation of one or two cracks. This is because the dimensionless stress intensity is inversely proportional to the internal pressure, P

$$K_I^* = \frac{K_I}{P\sqrt{\pi a}} \tag{10}$$

Experimental observations of fracture near a circular cavity have been produced by Bowie and Freese (1972), Clifton *et al.* (1976) and Abou-Sayed (1977). Estimates of the fracture toughness were produced using internally pressurized pre-notched hollow cylinders from what was called a "burst test." It is important to note that specimens were jacketed so that pressurizing fluid did not penetrate the crack, as in conventional hydraulic fracture experiments. Clifton *et al.* (1976) based the fracture toughness on extrapolation from a numerical analysis performed by Bowie and Freese (1972) for a specified geometry ($b/a = 8$). They observed stable crack growth in PMMA specimens and found $K_{Ic} = 0.810\ MPa\sqrt{m}$, which was comparable to other values of K_{Ic} for cast PMMA (McClintock 1966). Abou-Sayed (1977) extended this same type of testing and analysis to Indiana limestone and found that $K_{Ic} = 0.80MPa\sqrt{m}$, which was slightly below a previously measured fracture toughness value using a three-point-bending technique on Indiana Limestone (Schmidt and Huddle, 1976). They also observed that fracture toughness increases considerably with the application of confining pressure. They found that under 6.4 MPa of confinement, K_{Ic} increased by 80%.

Typical fracture experiments often rely on a notch to mimic a "starter" crack and from which fracture properties can then be measured. In this work, creating a notch from the borehole of the specimen was not attempted. However, it is clear that a fracture initiates near the boundary of a circular cavity prior to peak internal pressure. In every case, it was observed that two diametrically opposed radial cracks were produced.

2.4 Digital Image Correlation

Digital image correlation (DIC) is a particle-tracking technique that uses digital images to generate displacement fields. The technique stemmed from earlier work during the 1960's that introduced laser speckles as a tool for observing displacements. The laser speckle, generated by shining a laser on the surface of a specimen, has a unique size, shape, and intensity that are products of the local microscopic imperfections. When the specimen deforms, the speckles move and the surface displacement can be tracked by evaluating the movement of the speckle (Yamaguchi, 1981).

Extensive numerical analysis is required to estimate the speckle movement from the reference image (undeformed surface) to the current image (deformed surface). The process attempts to track small regions, called subsets, by performing correlation analysis between the two images (Peters & Ranson, 1982). The location of maximum correlation between the reference image and the current image coincides with the location of the displaced subset. Many algorithms, with slightly different correlation functions, have been introduced that use methods such as coarse-fine search (Sutton *et al.* 1983), Newton-Raphson (Bruck *et al.* 1989) and Fast Fourier Transform (Chen *et al.* 1993).

2.3.1 DIC Basics

One of the great advantages for using DIC is the ease of setup, which only requires a camera, lens, image acquisition system, and a software package or code that can perform the numerical correlation. The camera is setup perpendicular to the specimen and the lens is focused to ensure a clear image. The specimen is typically painted with black and white paint to create speckles. During an experiment, images of the specimen are taken before and

after deformation. The camera converts the light energy into a digital image that consists of many small squares called pixels. The total number of pixels per image is commonly called the resolution, which varies depending on the camera. During the image acquisition process, each pixel is assigned a digital value, called a grayscale value, which is related to the amount of light energy at that location. Grayscale values for an eight bit digital image range from 0-255, where extremely bright (white) pixels have higher grayscale values than dark (black) pixels.

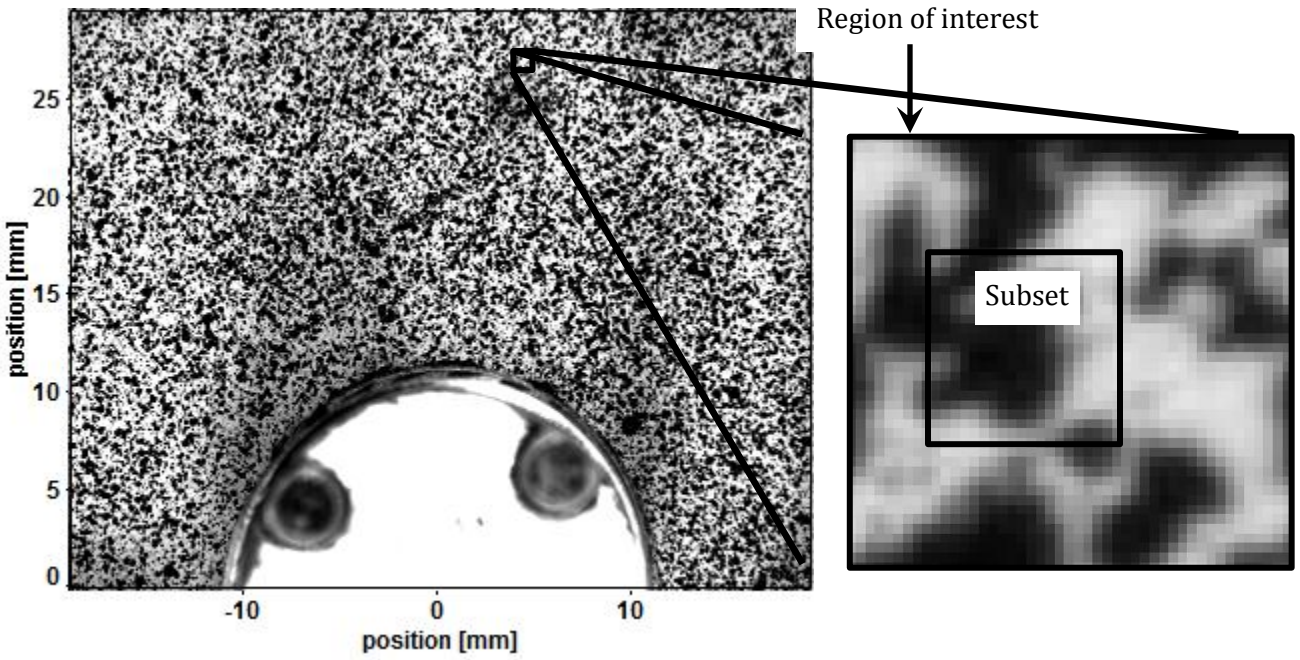

Figure 6: *(Left) a grayscale image of specimen with centered hole. (Right)Zoomed-in view of a region of interest (ROI) and a subset used for DIC analysis*

Figure 6 displays an image of a specimen with painted speckles that was taken during a cavity expansion experiment. The resolution of the image is 1600x1200 pixels and each pixel has a grayscale value from 0-255. There are nearly 2 million pixels in this image and only 255 different grayscale values, which means there are many pixels with the same

grayscale value. This makes it impossible to track individual pixels. Instead, groups of pixels, called subsets, are tracked that have a unique pattern of grayscale values. The size of the subset is set by the user and typically ranges from 20x20 pixels to 128x128 pixels.

The objective is to scan the current image to find the new location of the displaced subset. The displacements can be very small and it is not necessary to scan the entire image to locate the subset. Instead, the user specifies another parameter, called the region of interest (ROI), which is a region, many times smaller than the entire image, where the algorithm scans for the displaced subset. Restricting the scanning area substantially increases the speed of the correlation process. Figure 6 also shows a zoomed-in view of a region of interest that is almost four times larger than the subset but still very small in relation to the entire image.

The user has control of many different parameters that impact the analysis. Depending on the desired accuracy, speed or expected deformation, the parameters can be adjusted to meet the specific needs. For more accurate analysis, the software can perform a multi-pass method where multiple iterations are performed. The resulting vector field from the first iteration is passed into the second iteration as a reference field. The software also allows for overlap between subsets so that a higher resolution (vectors/area) is achieved without decreasing the size of the subsets. Larger subsets are advantageous because they have a pattern with more information (more pixels) and thus the measured displacement is more precise. Post-processing or filtering of the vector field can also be performed to smooth and create a continuous vector field.

Chapter 3

Cavity Expansion Test

The cavity expansion test pressurizes a central borehole in a cubic specimen. The applied internal pressure acts uniformly along the entire length of the borehole and as a result, a uniform two dimensional (2D) stress field develops along the axis of the borehole. The uniform distribution of internal pressure simplifies the three-dimensional problem to a plane-strain problem.

3.1 Loading Configurations

To produce a fracture from a circular cavity three different, 2D conditions were considered. The first and most simple condition was a circular hole subjected to internal pressure. The second condition was a circular hole subjected to internal pressure and far-field principal stresses. The third condition was a circular hole subjected to an arbitrary distribution of tractions along the boundary. The theoretical framework in the context of linear elasticity is developed in the proceeding sections.

Elasticity problems can be solved quickly by using the complex variable method developed by Kolosov (1909) and Muskhelishvili (1963). In the complex variable method, the Airy stress function, *U(x,y)*, can be written in terms of two analytic functions which depend on the complex variable *z*:

$$U(x,y) = \mathbf{Re}\left[\bar{z}\phi(z) + \int \psi(z)\right] dz \tag{11}$$

where $\phi(z)$ and $\psi(z)$ are themselves complex and are often referred to as *complex potentials*; *z* is the complex number formally written as *z = x + iy* and the over bar

represents the complex conjugate. The relationships between the Airy stress function and the stresses are

$$\sigma_x = \frac{\partial^2 U}{\partial y^2} \qquad \sigma_y = \frac{\partial^2 U}{\partial x^2} \qquad \sigma_{xy} = -\frac{\partial^2 U}{\partial x \partial y} \tag{12}$$

Combinations of the stress components from (12) can be solved as functions of the complex potentials in (11):

$$\sigma_x + \sigma_y = 4\mathbf{Re}\{\phi'(z)\} \tag{13}$$

$$\sigma_y - \sigma_x + 2i\sigma_{xy} = 2[\overline{z}\phi''(z) + \psi'(z)] \tag{14}$$

The displacement components (u_x, u_y) can be determined from elastic equations that relate the partial derivatives of the displacements to the stresses:

$$8G\frac{\partial u_x}{\partial x} = (\kappa + 1)\sigma_x + (\kappa - 3)\sigma_y \tag{15}$$

$$8G\frac{\partial u_y}{\partial y} = (\kappa + 1)\sigma_y + (\kappa - 3)\sigma_x \tag{16}$$

where κ is a coefficient for plane strain or plane stress:

$$\kappa = 3 - 4\nu \qquad \textit{for plane strain} \tag{17}$$

$$\kappa = \frac{3 - \upsilon}{1 + \upsilon} \qquad \textit{for plane stress} \tag{18}$$

The displacements are found from the following relationship:

$$2G\left(u_x + iu_y\right) = -\left(\frac{\partial U}{\partial x} + i\frac{\partial U}{\partial y}\right) + (\kappa + 1)\phi(z) \tag{19}$$

From (19) the displacements are

$$2G\left(u_x + iu_y\right) = \kappa\phi(z) - z\overline{\phi'(z)} - \overline{\psi(z)} \tag{20}$$

In polar coordinates, $z = re^{i\theta}$ and $e^{i\theta} = cos\theta + isin\theta$. Therefore, the displacements in polar coordinates are

$$2G(u_r + iu_\theta) = 2G\big(u_x + iu_y\big)e^{-i\theta} = \big[\kappa\phi(z) - z\overline{\phi'(z)} - \overline{\psi(z)}\big]e^{-i\theta} \tag{21}$$

Similarly, the stresses in polar coordinates are

$$\sigma_r + \sigma_\theta = \sigma_x + \sigma_y = 4\mathbf{Re}\{\phi'(z)\} \tag{22}$$

$$\sigma_\theta - \sigma_r + 2i\sigma_{r\theta} = \big(\sigma_y - \sigma_x + 2i\sigma_{xy}\big)e^{2i\theta} = 2[\bar{z}\phi''(z) + \psi'(z)]e^{2i\theta} \tag{23}$$

Circular Hole Subjected to Internal Pressure

Consider a 2D hollow cylinder with inner radius *a* and outer radius *b*. The complex potentials for this problem take the form (Jaeger & Cook, 1969),

$$\psi(z) = \frac{d}{z} \qquad\qquad \phi(z) = cz \tag{24}$$

where *c* and *d* are constants that can be imaginary or real; for the this problem with radial symmetry the constants are real. The *polar* complex displacement equation is found from (21) and (24):

$$2G(u_r + iu_\theta) = (\kappa - 1)cr - \frac{d}{r} \tag{25}$$

Separating the real and imaginary terms shows that

$$2Gu_r = (\kappa - 1)cr - \frac{d}{r}, \qquad 2Gu_\theta = 0 \tag{26}$$

The stresses are found from (22) and (23) using the complex potentials in (24):

$$\sigma_r + \sigma_\theta = 4c \tag{27}$$

$$\sigma_\theta - \sigma_r + 2i\sigma_{r\theta} = -\frac{2d}{r^2} \tag{28}$$

Separating the real and imaginary parts in (28) gives

$$\sigma_r - \sigma_\theta = -\frac{2d}{r^2}, \qquad \sigma_{r\theta} = 0 \tag{29}$$

The boundary conditions are such that $\sigma_r(a) = P_i$ and $\sigma_r(b) = 0$; the imposition of the boundary conditions with (27) and (29) allows the constants *c* and *d* to be solved:

$$c = -\frac{a^2 P_i}{2(b^2 - a^2)}, \quad d = -\frac{a^2 b^2 P_i}{(b^2 - a^2)} \tag{30}$$

The solution for the radial displacement and radial and tangential stress is found by substituting (30) into (26), (27) and (29):

$$2Gu_r = -(\kappa - 1)\frac{a^2 P_i r}{2(b^2 - a^2)} - \frac{a^2 b^2 P_i}{(b^2 - a^2)r} \tag{31}$$

$$\sigma_r = -\frac{a^2 P_i}{(b^2 - a^2)} + \frac{a^2 b^2 P_i}{(b^2 - a^2)r^2} \tag{32}$$

$$\sigma_\theta = -\frac{a^2 P_i}{(b^2 - a^2)} - \frac{a^2 b^2 P_i}{(b^2 - a^2)r^2} \tag{33}$$

The solution for a hole in an infinite mass is found by taking the limit as b $\longrightarrow\infty$. The results for the case of plane strain are

$$2Gu_r = P_i\left(\frac{a^2}{r}\right) \tag{34}$$

$$\sigma_r = P_i\left(\frac{a}{r}\right)^2 \tag{35}$$

$$\sigma_\theta = -P_i\left(\frac{a}{r}\right)^2 \tag{36}$$

Circular Hole subjected to Internal Pressure and Far Field Stress

The solution for a circular hole subjected to far field normal stress was first solved by the German engineer E.G. Kirsch in 1898. The complex potential method will again be used to solve for the stress and displacement fields (Jaeger & Cook, 1969):

$$\phi(z) = \frac{1}{4}\sigma_1^{\infty}\left(z + \frac{A}{z}\right) \tag{37}$$

$$\psi(z) = -\frac{1}{2}\sigma_1^{\infty}\left(z + \frac{B}{z} + \frac{C}{z^3}\right) \tag{38}$$

where *A*, *B,* and *C* are real constants. The combinations of radial and tangential stresses are found from (22)and (23):

$$\sigma_r + \sigma_\theta = 4\mathbf{Re}\{\phi'(z)\} = \sigma_1^{\infty}(1 - Ar^{-2}cos2\theta) \tag{39}$$

$$\begin{aligned}\sigma_\theta - \sigma_r + 2i\sigma_{r\theta} &= 2\left[\bar{z}\phi''(z) + \psi'(z)\right]e^{2i\theta}\right] \\ &= \sigma_1^{\infty}\left[Br^{-2} - e^{2i\theta} + (1 - Ar^{-2} - 3Cr^{-4})e^{-2i\theta}\right]\end{aligned} \tag{40}$$

The tangential and radial stresses are solved from (39) and the real part of (40):

$$\sigma_\theta = \frac{1}{2}\sigma_1^{\infty}[1 + Br^{-2} + (3Cr^{-4} - 1)cos2\theta] \tag{41}$$

$$\sigma_r = \frac{1}{2}\sigma_1^{\infty}[1 - Br^{-2} + (1 - 2Ar^{-2} - 3Cr^{-4})cos2\theta] \tag{42}$$

The imaginary part of (40) gives the shear stress:

$$\sigma_{r\theta} = -\frac{1}{2}\sigma_1^{\infty}[(1 - 2Ar^{-2} - 3Cr^{-4})sin2\theta] \tag{43}$$

The solutions to the constants are found from the boundary condition where the stresses vanish at the boundary of the hole *(r = a)*.

$$A = 2a^2 \qquad B = a^2 \qquad C = -a^4 \tag{44}$$

The full expressions for the stresses are

$$\sigma_\theta = \frac{1}{2}\sigma_1^\infty \left[1 + \left(\frac{a}{r}\right)^2\right] - \frac{1}{2}\sigma_1^\infty \left[1 + \left(\frac{a}{r}\right)^4\right] cos2\theta \quad (45)$$

$$\sigma_r = \frac{1}{2}\sigma_1^\infty \left[1 - \left(\frac{a}{r}\right)^2\right] + \frac{1}{2}\sigma_1^\infty \left[1 - 4\left(\frac{a}{r}\right)^2 + 3\left(\frac{a}{r}\right)^4\right] cos2\theta \quad (46)$$

$$\sigma_{r\theta} = -\frac{1}{2}\sigma_1^\infty \left[1 + 2\left(\frac{a}{r}\right)^2 - 3\left(\frac{a}{r}\right)^4\right] sin2\theta \quad (47)$$

The stress due to a second far-field stress, σ_2^∞ can be found from (45)-(47) by replacing 2θ with $2\theta + \pi$. The full state of stress around a hole can then be found by superposing the two solutions. Also, if the borehole is subjected to internal pressure, then the state of stress is found by superposing (45)-(47) with (35) and (36). The full state of stress including the addition of a second normal stress and internal borehole pressure is

$$\sigma_\theta = \frac{1}{2}(\sigma_1^\infty + \sigma_2^\infty)\left[1 + \left(\frac{a}{r}\right)^2\right] - P\left(\frac{a}{r}\right)^2 - \frac{1}{2}(\sigma_1^\infty - \sigma_2^\infty)\left[1 + \left(\frac{a}{r}\right)^4\right] cos2\theta \quad (48)$$

$$\sigma_r = \frac{1}{2}(\sigma_1^\infty + \sigma_2^\infty)\left[1 - \left(\frac{a}{r}\right)^2\right] + P\left(\frac{a}{r}\right)^2 + \frac{1}{2}(\sigma_1^\infty - \sigma_2^\infty)\left[1 - 4\left(\frac{a}{r}\right)^2 + 3\left(\frac{a}{r}\right)^4\right] cos2\theta \quad (49)$$

$$\sigma_{r\theta} = -\frac{1}{2}(\sigma_1^\infty - \sigma_2^\infty)\left[1 + 2\left(\frac{a}{r}\right)^2 - 3\left(\frac{a}{r}\right)^4\right] sin2\theta \quad (50)$$

The tangential stress varies from a minimum value of $3\sigma_2^\infty - \sigma_1^\infty - P$ when $\theta = 0$ or π and a maximum value of $3\sigma_1^\infty - \sigma_2^\infty - P$ when $\theta = \pi/2$ or $3\pi/2$. A region of tensile tangential stress will exist if

$$P > 3\sigma_2^\infty - \sigma_1^\infty \quad (51)$$

This is the criteria for hydraulic fracture initially developed by Hubbert and Willis (1957).

The displacement field is found by solving (21) using (37) and (38) and the results for constants *A*, *B* and *C*. The radial and tangential displacements for a hole subjected to a single far-field stress are

$$\frac{8Gu_r}{a\sigma_1^\infty} = \left[(\kappa-1)\left(\frac{r}{a}\right) + 2\left(\frac{a}{r}\right)\right] + 2\left[\left(\frac{r}{a}\right) + (\kappa+1)\left(\frac{a}{r}\right) - \left(\frac{a}{r}\right)^3\right] cos2\theta \tag{52}$$

$$\frac{8Gu_\theta}{a\sigma_1^\infty} = -2\left[\left(\frac{r}{a}\right) + (\kappa-1)\left(\frac{a}{r}\right) + \left(\frac{a}{r}\right)^3\right] sin2\theta \tag{53}$$

The change in radius of the hole is found by evaluating (52) and (53) at $r = a$:

$$\frac{u_r(a)}{a} = \frac{(\kappa+1)\sigma_1^\infty}{8G}[1 + 2cos2\theta] \tag{54}$$

$$\frac{u_\theta(a)}{a} = -\frac{(\kappa+1)\sigma_1^\infty}{4G}[sin2\theta] \tag{55}$$

Circular Hole Subjected to an Arbitrary Distribution of Tractions

The problem of a circular cavity subjected to an arbitrary distribution of tractions is shown in Figure 7. Uniform pressure P is applied to two symmetric arcs, $-\alpha < \theta < \alpha$ and $\pi-\alpha > \theta > \pi+\alpha$. The solution to this problem is more involved than the preceding problems, and requires analysis by infinite Fourier series (Jaeger and Cook, 1969). The derivatives of the complex potentials are given in terms of a power series as

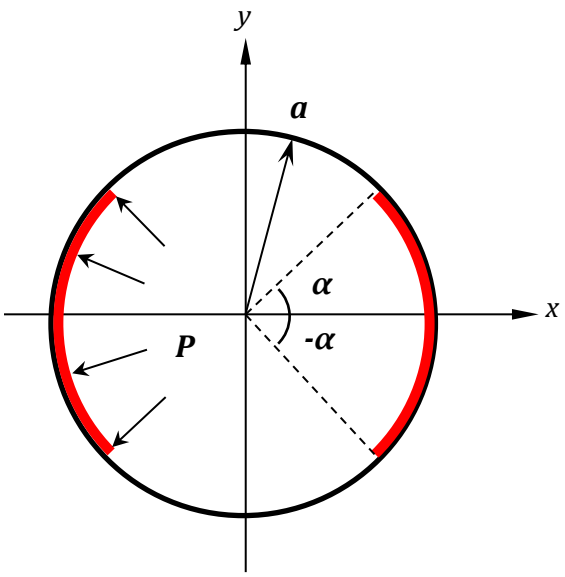

Figure 7: Circular hole loaded with pressure P over two symmetric arcs (red).

$$\phi'(z) = \sum_{n=2}^{\infty} c_n z^{-n} \tag{56}$$

$$\psi'(z) = \sum_{n=2}^{\infty} d_n z^{-n} \tag{57}$$

The coefficients c_n and d_n are solved from the boundary conditions at $r = a$. The boundary conditions describe the normal and shear tractions along the boundary of the hole and are an infinite series that depends on the angular distribution of loading. Specifically, the boundary conditions are

$$N - iT = \sum_{n=-\infty}^{\infty} A_n e^{in\theta} \tag{58}$$

N is the normal traction and *T* is the shear traction. The coefficients A_n are zero along the unloaded region and along the loaded region are found by solving the Fourier series and are related to the complex potential's constants, c_n and d_n (Jaeger and Cook, 1969):

$$c_{2m} = \left(\frac{Pa^{2m}}{m\pi}\right) sin2m\alpha \tag{59}$$

$$d_2 = \frac{-2P\alpha a^2}{\pi}$$

$$d_{2m+2} = \left(\frac{2Pa^{2m+2}}{\pi}\right) sin2m\alpha \qquad m = 1,2,3..... \tag{60}$$

Inserting (59) and (60) into (56) and (57) gives

$$\phi'(z) = \frac{P}{\pi}\sum_{m=1}^{\infty} \frac{sin2m\alpha}{m}\left(\frac{a}{z}\right)^{2m} \tag{61}$$

$$\psi'(z) = -\frac{2P\alpha}{\pi}\left(\frac{a}{z}\right)^{2} + \frac{2P}{\pi}\sum_{m=1}^{\infty} sin2m\alpha \left(\frac{a}{z}\right)^{2m+2} \tag{62}$$

The stresses are found by substituting (61) and (62) into (22) and (23):

$$\sigma_r = \frac{2P\alpha}{\pi}\left(\frac{a}{r}\right)^{2} + \frac{2P}{\pi}\sum_{m=1}^{\infty}\left(\frac{a}{r}\right)^{2m}\left[\frac{1+m}{m} - \left(\frac{a}{r}\right)^{2}\right] sin2m\alpha\ cos2m\theta \tag{63}$$

$$\sigma_\theta = -\frac{2P\alpha}{\pi}\left(\frac{a}{r}\right)^{2} + \frac{2P}{\pi}\sum_{m=1}^{\infty}\left(\frac{a}{r}\right)^{2m}\left[\frac{1-m}{m} + \left(\frac{a}{r}\right)^{2}\right] sin2m\alpha\ cos2m\theta \tag{64}$$

$$\sigma_{r\theta} = \frac{2P}{\pi}\left[1 - \left(\frac{a}{r}\right)^{2}\right]\sum_{m=1}^{\infty} sin2m\alpha\ sin2m\theta \left(\frac{a}{r}\right)^{2m} \tag{65}$$

At the boundary *r = a*, the stresses are

$$\sigma_r(a) = \frac{2P\alpha}{\pi} + \frac{2P}{\pi}\sum_{m=1}^{\infty}\frac{sin2m\alpha\ cos2m\theta}{m} \tag{66}$$

$$\sigma_\theta(a) = -\frac{2P\alpha}{\pi} + \frac{2P}{\pi}\sum_{m=1}^{\infty}\frac{sin2m\alpha\ cos2m\theta}{m} \tag{67}$$

$$\sigma_{r\theta}(a) = 0 \tag{68}$$

At the boundary, the tangential stress reduces considerably by noting that the right-hand side of (66) must sum to *P* in the loaded region and to zero in the unloaded region. This allows the summation to be solved and the tangential stress is

$$\sigma_\theta = P - \frac{4\alpha P}{\pi} \qquad \textit{along loaded region} \tag{69}$$

$$\sigma_\theta = -\frac{4\alpha P}{\pi} \qquad \textit{along unloaded region} \tag{70}$$

This shows that a maximum *tensile* tangential stress develops at the boundary of the hole along the unloaded region.

The displacements are found by integrating the complex potentials in (61) and (62):

$$\phi(z) = -\frac{P}{\pi}\sum_{m=1}^{\infty}\frac{sin2m\alpha}{m(2m-1)}a\left(\frac{a}{z}\right)^{2m-1} \tag{71}$$

$$\psi(z) = \frac{2P\alpha}{\pi}\frac{a^2}{z} - \frac{2P}{\pi}\sum_{m=1}^{\infty}\frac{sin2m\alpha}{2m+1}a\left(\frac{a}{z}\right)^{2m+1} \tag{72}$$

The radial and tangential displacements are found by substituting (61), (71) and (72) into (21):

$$2Gu_r = -\frac{2P\alpha}{\pi}\frac{a^2}{r} - \frac{P}{\pi}\sum_{m=1}^{\infty}\left(\frac{a}{r}\right)^{2m}\left[\frac{2}{2m+1}\frac{a^2}{r} + \frac{2\kappa}{2m-1}r - \frac{r}{m}(\kappa+1)\right]sin2m\alpha\ cos2m\theta \tag{73}$$

$$2Gu_\theta = -\frac{P}{\pi}\sum_{m=1}^{\infty}\left(\frac{a}{r}\right)^{2m}\left[\frac{2}{2m+1}\frac{a^2}{r} + \frac{2\kappa}{2m-1}r - \frac{r}{m}(\kappa+1)\right]sin2m\alpha\ sin2m\theta \tag{74}$$

At the boundary *r = a*, the radial and tangential displacements reduce to

$$2Gu_r(a) = -\frac{2P\alpha}{\pi}a - \frac{Pa}{\pi}\sum_{m=1}^{\infty}\frac{1}{m}\left[\frac{\kappa}{2m+1} + \frac{2}{2m-1}\right] sin2m\alpha\ cos2m\theta \tag{75}$$

$$2Gu_\theta(a) = -\frac{Pa}{\pi}\sum_{m=1}^{\infty}\frac{1}{m}\left[\frac{\kappa}{2m+1} + \frac{2}{2m-1}\right] sin2m\alpha\ sin2m\theta \tag{76}$$

Solutions for the stresses and displacements involve solving an infinite series. Exact solutions for the displacement and stress field are available at the boundary wall for $\theta = 0, \pi/2, 3\pi/2$ and π (Bray, 1987; Jaeger and Cook, 1969). However, solutions away from the boundary ($r > a$) require summing the series until it converges.

Figure 8 shows the radial stress plotted for various values of α and $\theta = \pi/2$. The plot shows the radial stress normalized by the internal pressure (σ_r/P) versus the dimensionless position, r/a, where a is the radius of the hole. The radial and tangential stresses from (63) and (64) were solved by truncating the series once it converged. Figure 9 shows the plot for tangential stress. Notice that at the boundary the tangential stress σ_θ is greater than the internal pressure for values of α that are greater than 45°.

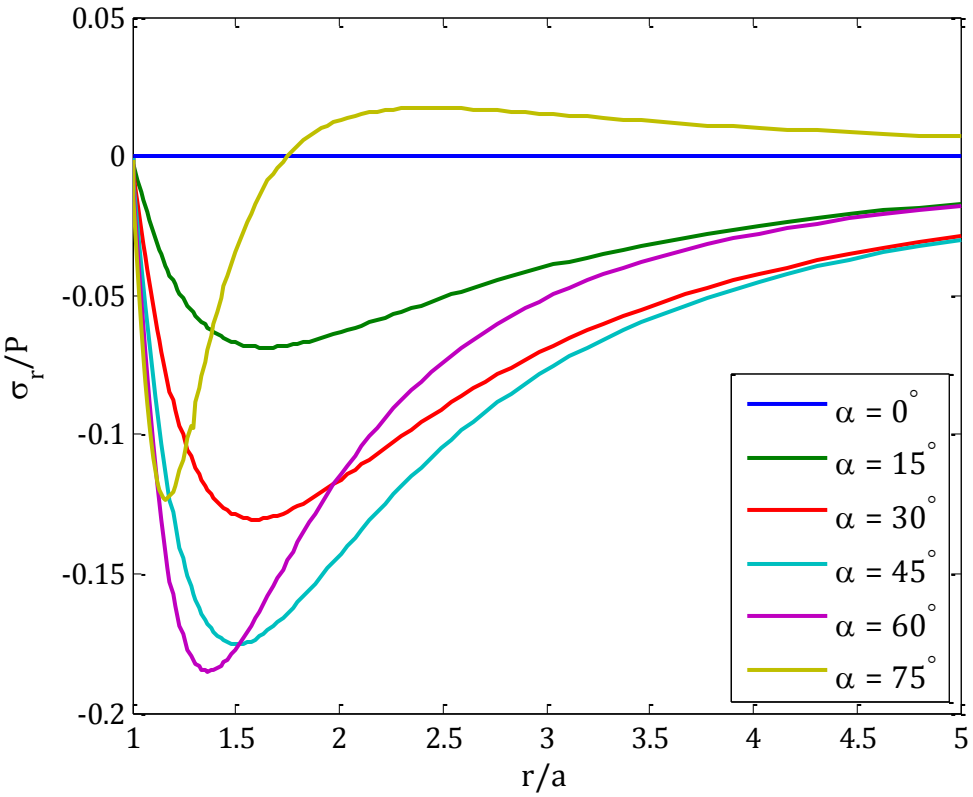

Figure 8: Radial stress plotted for various angular distributions of internal pressure.

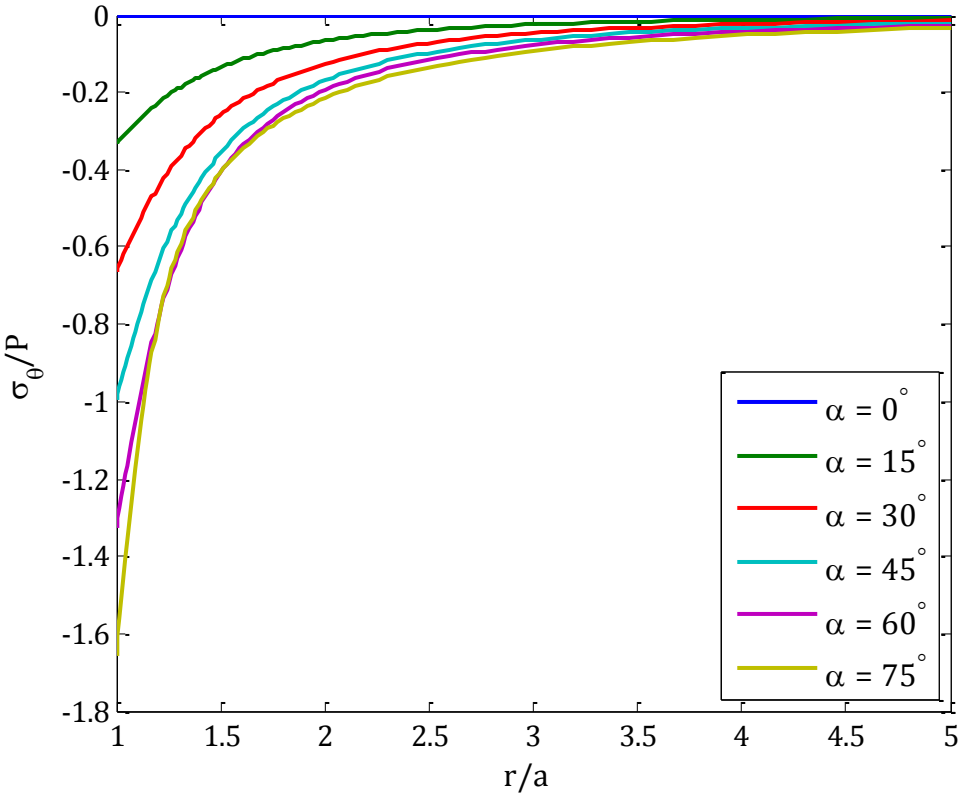

Figure 9: Tangential stress plotted for various angular distributions of internal pressure.

3.2 Cavity Expansion Apparatus

The cavity expansion apparatus (CEA) was designed to monitor displacements on a surface near an internally pressurized circular cavity. The CEA consists of the axial loading cell (ACL), a reaction frame for producing lateral stress on the specimen, and a urethane packer that produces the internal pressure in the cavity. Detailed descriptions of the constituent parts of the apparatus are given in the proceeding sections.

3.2.1 Load Frame Design

The CEA consists of an axial loading cell (ALC) housing a prismatic specimen (Figure 10). The ALC consists of four 19mm (¾ in.) threaded rod, fastened with 28.6mm (1-⅛ in.) fasteners to top and bottom square steel platens. The platens confine the specimen along the axis of the borehole and promote a zero displacement condition in that direction. Contacting the surface was produced by tightening the fasteners. The bottom platen has a center hole cut-out to allow for the insertion of the urethane packer. The top platens have a center rectangular window cut-out using electric discharge machining (EDM) to allow placement for a rectangular glass platen (Figure 11). The glass platen is necessary for viewing displacement on the specimen's surface with the DIC technique.

The glass platen is made of clear, 12.7mm (½ in.) thick annealed glass from Brin Northwestern Glass Company (Minneapolis, MN). The strength properties of the glass are generally much higher than those of the specimen. The glass platen has a 20mm centered hole cut-out for insertion of the urethane packer.

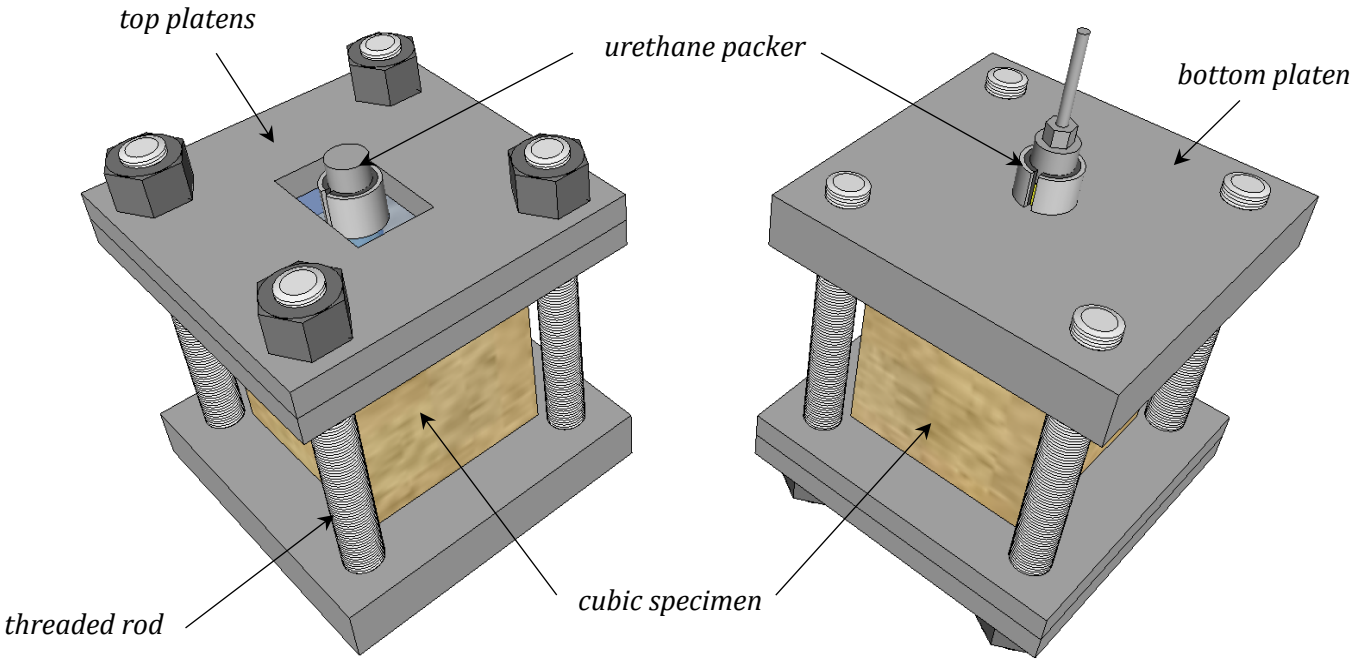

Figure 10: (Left) Axial loading cell (ALC) showing the top platens and glass platen for viewing displacements on the surface of the specimen. (Right) ALC showing bottom platen and packer insert in the middle.

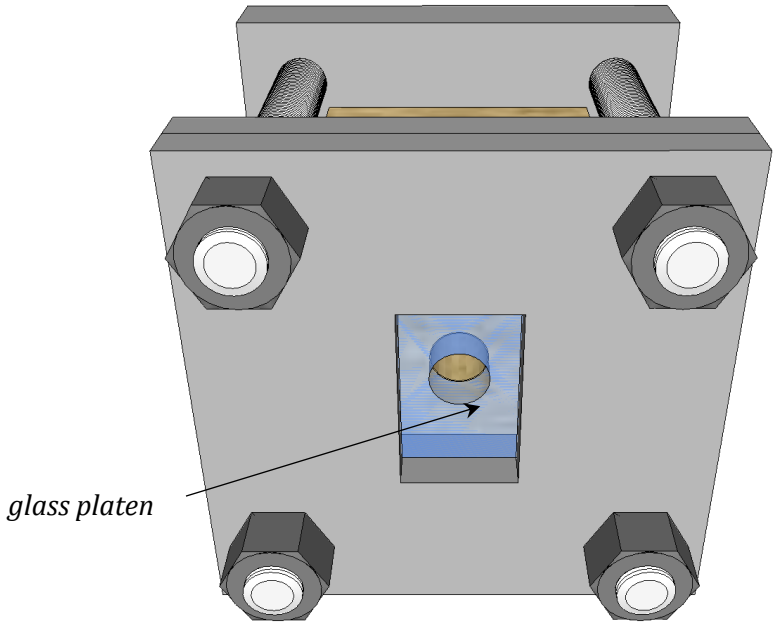

Figure 11: Glass platen with center hole inside the top platen

Insertion of side platens into the ALC allows for applied stress on the lateral surfaces of the specimen from hydraulic flat-jacks (Figure 12 and 13). All platens were made of precision surface ground steel. The hydraulic flat-jacks consist of two thin steel plates welded together along the edges with in-flow and out-flow high-pressure tubing welded to the corners of the flat-jack. A flat-jack does not produce uniform stress due to the edges being welded together; for typical flat-jacks it is assumed that the outer 6mm (¼ in.) perimeter of the flat-jack is inoperable (Amadei and Stephansson, 1997). Hydraulic fluid is pumped into the flat-jack to produce an applied stress on both sides of the flat-jack. The hydraulic loading is controlled by an electric motor pump and the system is monitored with a 70 MPa (10,000 psi) capacity strain-type pressure transducer. The system also has closed-loop feedback capabilities and can be held at a constant pressure throughout the test.

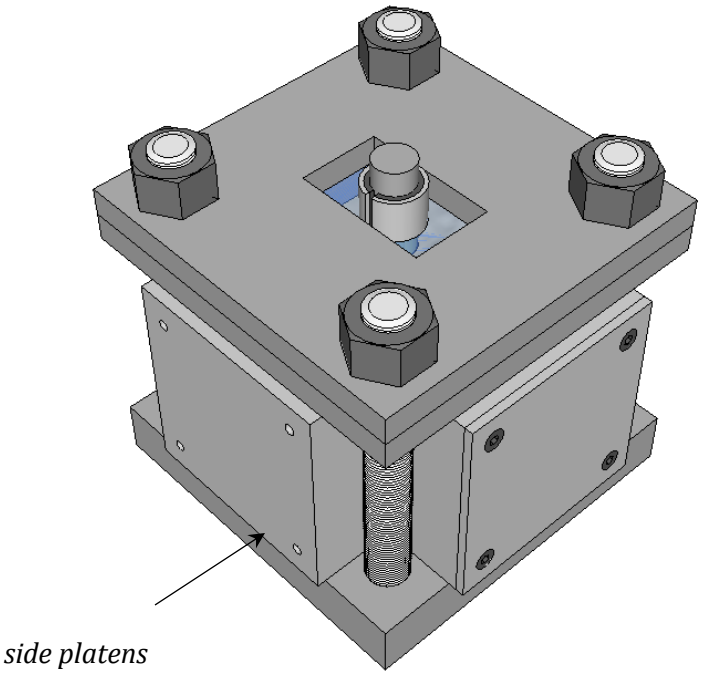

Figure 12: Axial loading cell (ALC) with top, bottom, and side platens.

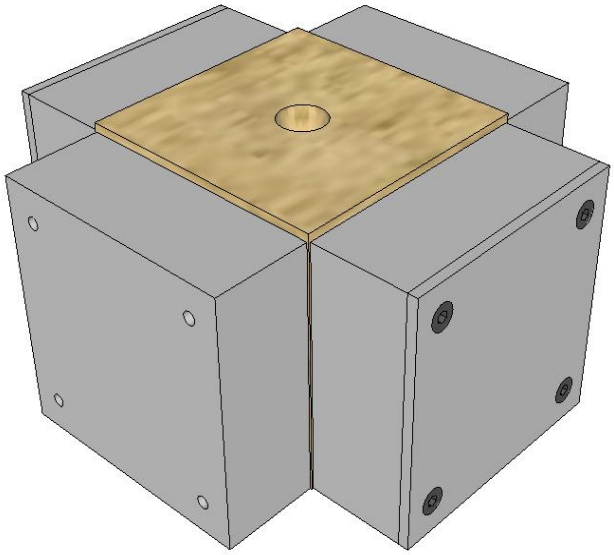

Figure 13: View of the specimen and side platens.

The surface area of a flat-jack was larger than the surface area of the platen that was in contact with the lateral surface of the specimen (Figure 14). Because of this difference in surface area, the applied stress on the specimen was increased by a factor that is equal to $A_{flat\text{-}jack}/A_{platen}$. This constant was equal to 2.67 for all experiments.

The CEA is shown in Figure 15 with the ALC placed in the center of the reaction frame. The reaction frame consists of four 50.8mm (2in.) thick, 381mm (15in.) diameter steel cylinders with an 203mm (8in.) square cut-out in the center (Figure 15). Each cylinder is stacked on top of the other creating a 203mm × 203mm × 203mm cubic space for placement of the ALC. An exploded view of the CEA is shown in Figure 16 with its constituent parts. Some parts have been left out in the schematic to help clarify the layout of the apparatus.

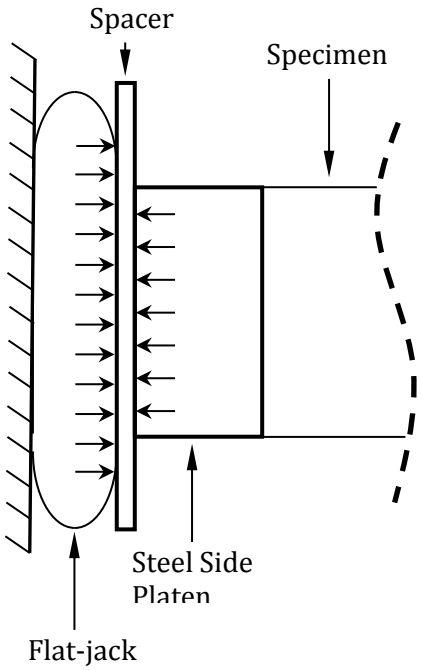

Figure 14:Cross-section view of flat-jack and side platens. The difference in surface area causes an increase in normal stress on the specimen.

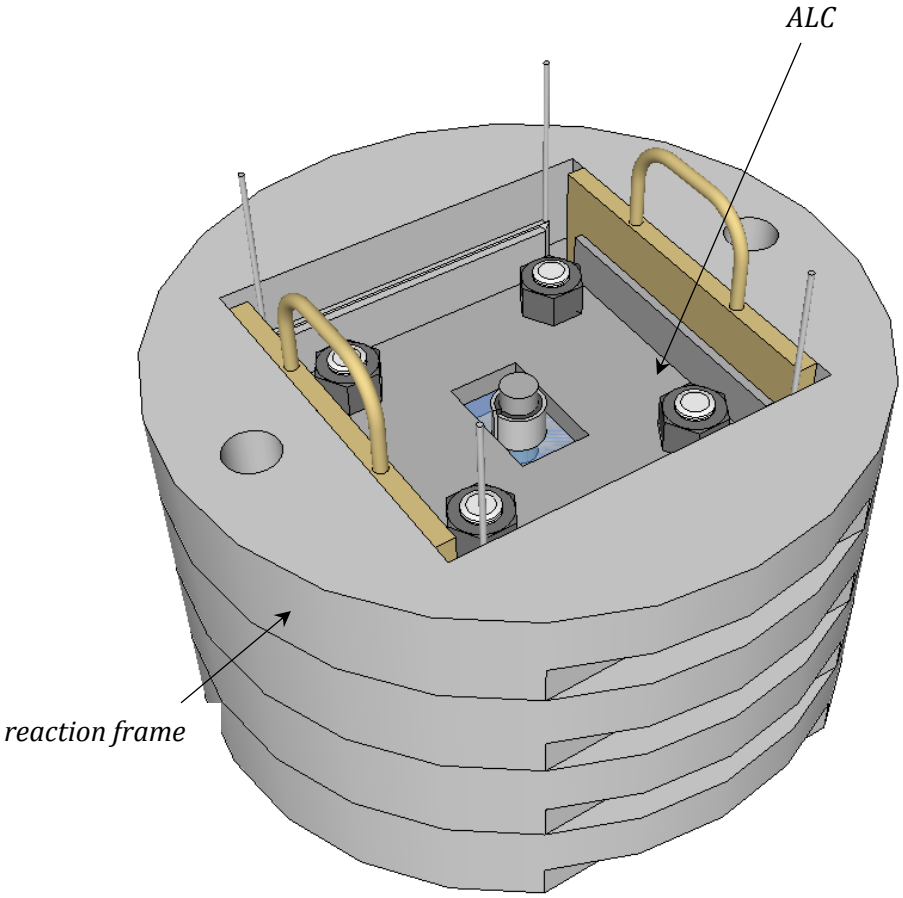

Figure 15: Reaction frame with ALC.

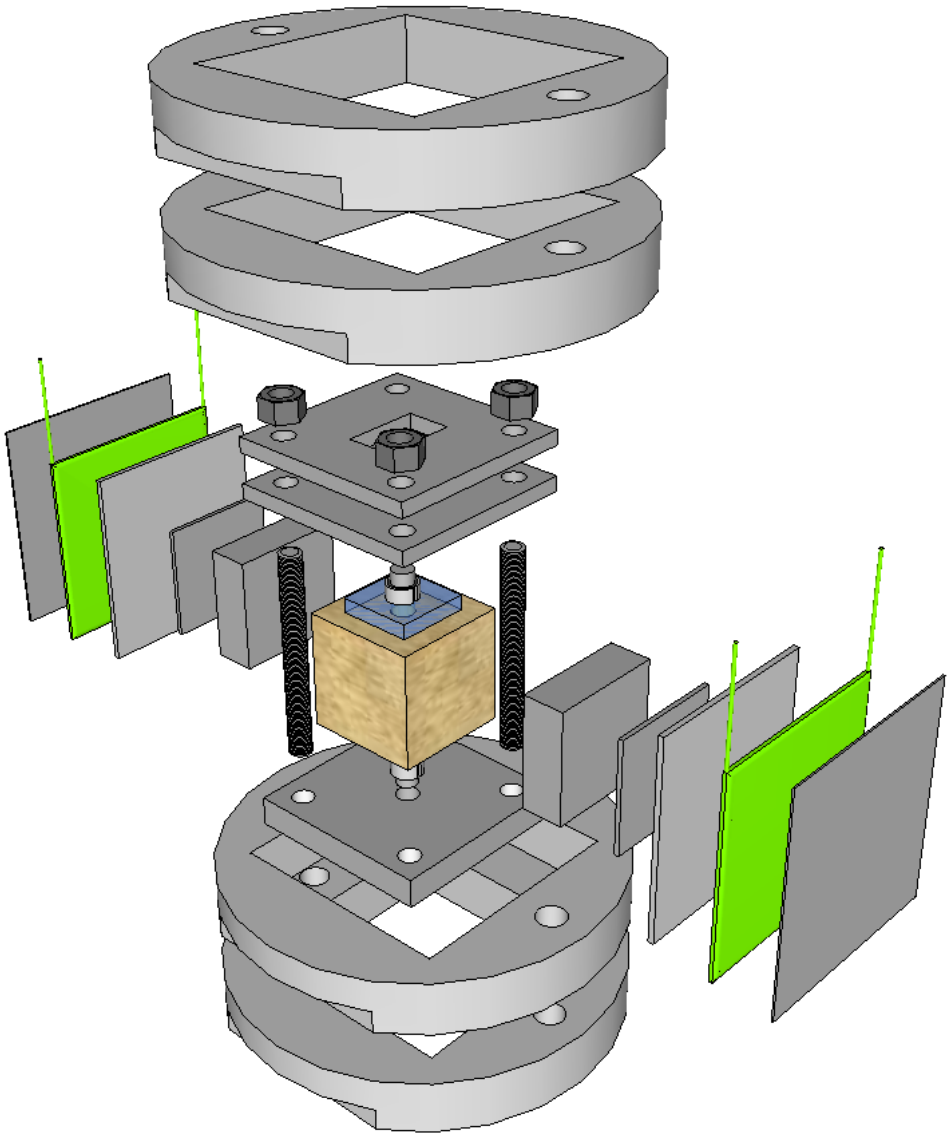

Figure 16: Exploded view of the reaction frame, ALC and urethane packer. The ALC consists of top, bottom and glass platens as well as threaded rods. The reaction frame consists of circular metal plates, lateral loading platens and hydraulic flat-jacks.

The CEA has a significant advantage for controlling where the fracture will initiate. If the location of fracture initiation is known *a priori*, then the DIC camera can be positioned to capture the images. In conventional fracture tests, such as a three-point-bending test, a notched specimen is usually used so that fracture will develop at a predetermined location. However, preparation of a notched specimen for the cavity expansion test would be difficult and time consuming. For an experiment using the CEA, the location of fracture initiation is dependent on the applied normal stresses. For brittle materials, the normal vector to the fracture plane points in the direction of least principal stress. Therefore, during a test, the magnitude and direction of applied far-field normal stress will determine where the fracture initiates and where it will propagate.

As an example, consider compressive stresses on a cube oriented in the directions as indicated in Figure 17. In Figure 17a, a vertical fracture plane parallel to the *z-axis* forms since the minimum stress σ_3 points in the *negative* y-direction. Furthermore, since the maximum lateral stress σ_1 is also known the location of fracture initiation is known. Notice, if $\sigma_1 = \sigma_3$ then the fracture could occur on any plane parallel to the *z-direction* (Figure 17b). If the state of stress is such as that depicted in Figure 17c, then fracture will initiate and propagate horizontally from the borehole and capturing fracture initiation at the borehole boundary would be impossible. For experiments using applied far-field stress to initiate fracture, the maximum stress was 3.5 – 7.0 *MPa* (500 – 1000 *psi*) and the minimum lateral stress was 0 *MPa*.

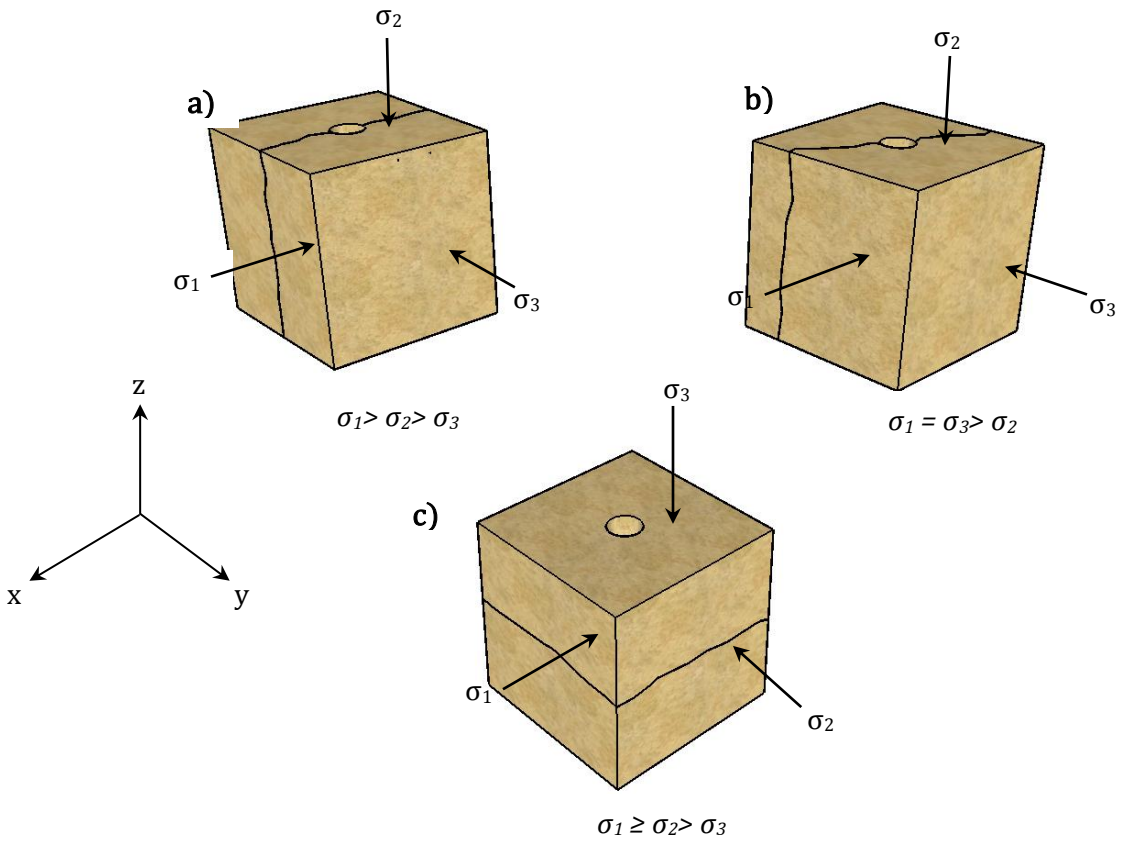

Figure 17: Three different orientations of the fracture plane. a) Vertical fracture plane with its normal vector pointing in the direction of σ_3. b) Fracture initiates on any plane parallel to the z-axis when $\sigma_1 = \sigma_3$. c) Horizontal fracture initiates since σ_3 points along the z-axis.

An alternative way of developing the location of fracture is by the use an arbitrary distribution of tractions along the boundary of the borehole wall (refer to section 3.1 for theoretical framework). Two thin (thickness = 0.3mm) aluminum spacers were inserted into the borehole between the urethane packer and the hole (Figure 18). The spacers were thin enough so that the

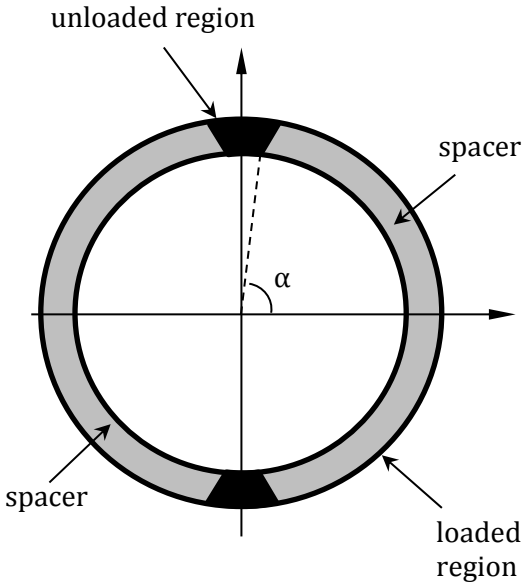

Figure 18: Plane view of spacers inserted in between the borehole and specimen.

radial stress at the boundary of the spacer and specimen was approximately equal to the internal pressure. However, the disjoint along the perimeter of the spacers produces a significant concentration of *tensile* tangential stress along the unloaded region. At the hole boundary, the concentration of tensile stress can be calculated from (70). For all experiments using an arbitrary distribution of tractions to produce fracture, the angular distribution of loading was $\alpha = 4\pi/9$ (80°) Therefore at $r = a$:

$$\sigma_\theta(a) = \frac{-4\alpha P}{\pi} \approx -1.78P \qquad 77)$$

The radial distribution of tangential stress normalized by the internal pressure for $\alpha = 4\pi/9$ (80°) and $\theta = \pi/2$ is shown in Figure 19.

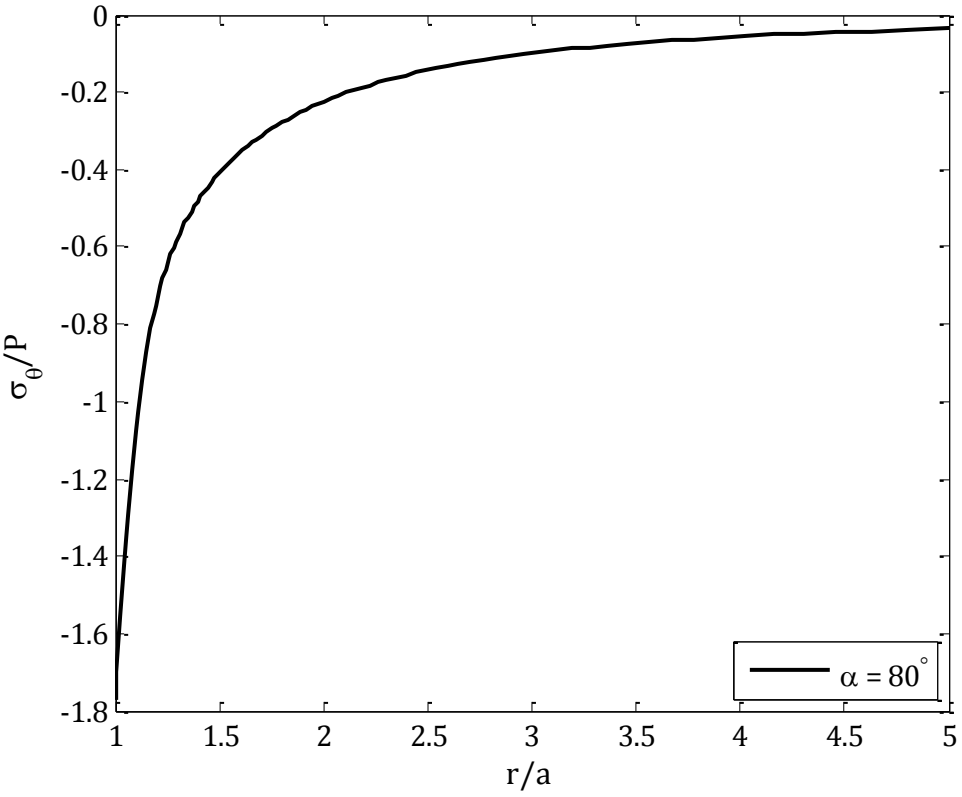

Figure 19: Radial distribution of tangential stress for an angular distribution of tractions along the borehole wall.

3.2.2 Urethane Packer Design

The urethane packer that supplies the internal pressure in the borehole is a traditional straddle packer encased in a urethane sleeve (Figure 20). The overall length of the packer is approximately 190mm, the pressurizing interval is 150mm and the diameter is 20mm. The physical properties of the urethane are discussed in section 4.2. The urethane packer keeps pressurizing fluid from penetrating the specimen and generates uniform pressure along the entire length of the borehole.

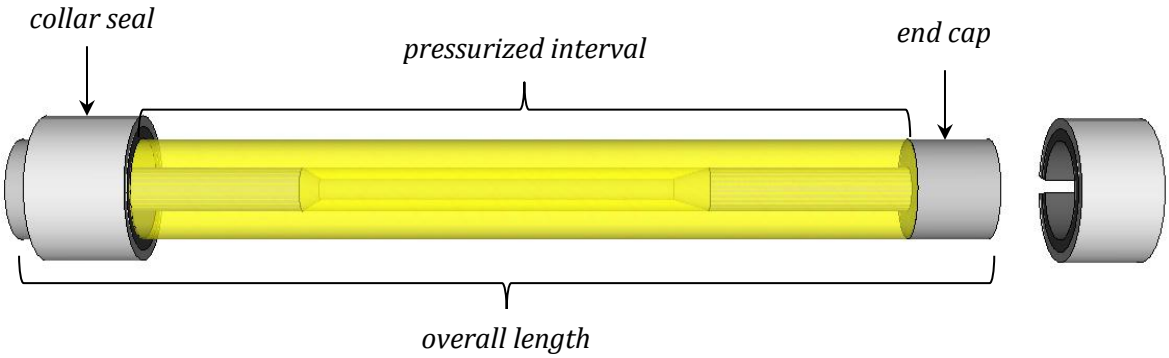

Figure 20: Urethane packer with end cap clamping seals.

The urethane packer is usually completely inserted into a borehole with both ends of the packer enclosed in the specimen. The ends of the packer are made of 20mm diameter metal end caps. The end caps generate zero stress on the borehole boundary and are only for confining the fluid inside the sleeve. However, for this 2D experiment, monitoring fracture had to be observed at the *pressurized* boundary of the borehole and packer, therefore modification of the urethane packer was necessary. In the borehole, the urethane packer contacts the entire 10cm length of the borehole, leaving 5cm of the packer in contact with the center holes in the top and bottom platens (Figure 12). The seals at either end of the

packer have deteriorated over time and were incapable of supporting pressure high enough to initiate fracture. Therefore, collar seals where placed on both ends of the packer, where the urethane joins the steel end caps, to allow for higher pressures in the packer (Figure 20).The internal pressure was monitored by a 35 MPa (5000 psi) BLH strain-type pressure transducer. The system also had closed-loop feedback capabilities to maintain a constant injection rate. Water was injected into the packer at a constant rate of 0.5-0.8 cc/min via a motor driven pumping system with closed-loop feedback capabilities until fracture was initiated.

3.2.3 DIC Monitoring

A charged coupled device (CCD) camera was positioned above the CEA to capture images throughout the test (Figure 21). The camera was mounted to a heavy steel arm and secured to a heavy metal base. This was used to reduce noise from vibration effects. The reaction frame is placed on a wooden stand to allow connection for the packers pressurizing tubes beneath the CEA. The digital camera used a firewire interface to communicate with a PC. The software used to capture images was Unibrain Fire-i 810b. The software can control the camera to capture images at a predefined rate and set the resolution and image size. For each test, 1 frame per second (FPS) was used with a grayscale 8-bit resolution and an image size of two megapixels (1200x1600 pixels).

Monitoring the packer-borehole boundary with the CCD camera could not be positioned directly perpendicular to the surface of the specimen because of the clamping seals described in section4.1.2 blocked the field of view. The camera was tilted less than 1° from the vertical axis of the borehole. Image distortion because of the tilt was considered to be negligible.

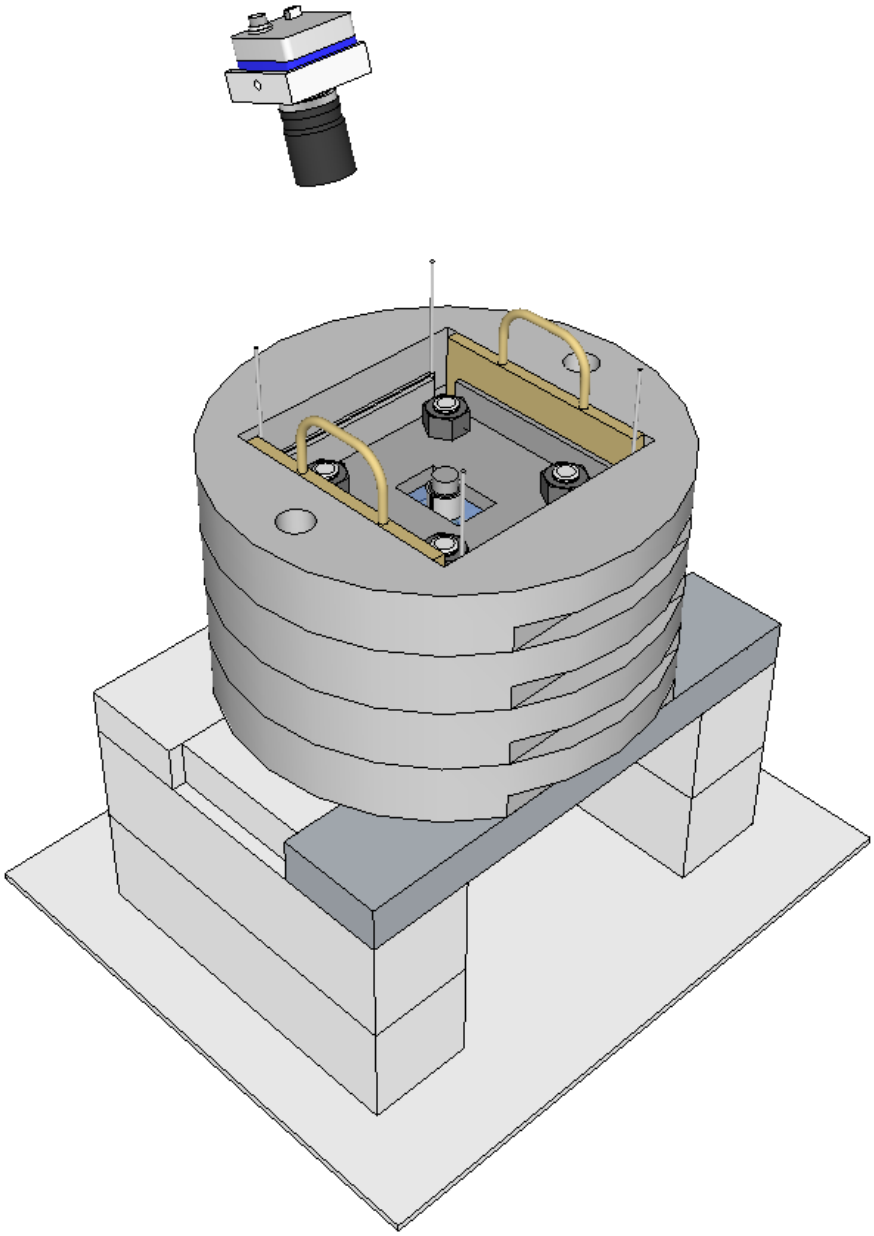

Figure 21: The CEA mounted on a wooden base. The CCD camera was mounted on a heavy metal arm above the CEA.

3.3 Calibration

The stresses associated with a sleeved packer in an elastic medium were solved by considering two hollow cylinders sharing the same axis of symmetry (concentric). Solutions for the stresses were found by considering the Lame solution reviewed in section 3.1.

Consider two concentric hollow cylinders subjected to internal pressure, P_i, and external pressure, P_o (Figure 22). Radial displacement, u_r, is continuous at the boundary $r = b$.

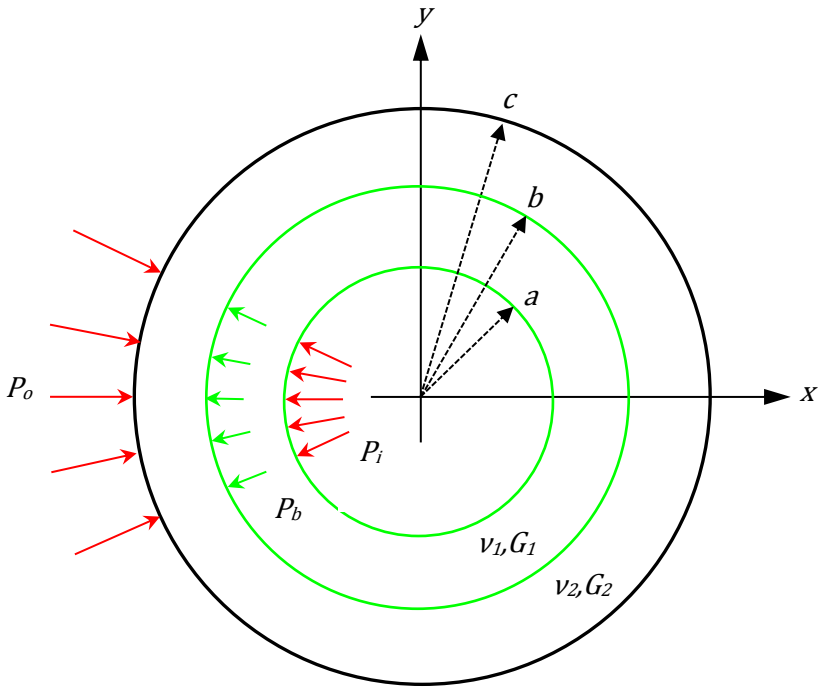

Figure 22: Two concentric hollow cylinders subjected to internal and external pressure

Depending on the material properties (G,ν) of the inner and outer cylinders as well as the radii of each cylinder, the boundary pressure, P_b, may be greater or less than the internal pressure, P_i.

The displacement at the boundary $r = b$ can be written as:

$$\frac{1-2\upsilon_1}{2G_1}\left(\frac{P_i a^2 - P_b b^2}{b^2-a^2}\right) + \frac{a^2(P_i - P_b)}{2G_1(b^2-a^2)} = \frac{1-2\upsilon_2}{2G_2}\left(\frac{P_b b^2 - P_o c^2}{c^2-b^2}\right) + \frac{c^2(P_b - P_o)}{2G_2(c^2-b^2)} \qquad (78)$$

Solving for P_b yields

$$P_b = \frac{2\left[P_i\, {a^2}/{b^2}\,(1-\upsilon_1)G_2\left(1-{b^2}/{c^2}\right) + P_o(1-\upsilon_2)G_1\left(1-{a^2}/{b^2}\right)\right]}{G_2\left((1-2\upsilon_1)+{a^2}/{b^2}\right)\left(1-{b^2}/{c^2}\right) + G_1\left((1-2\upsilon_1)\,{b^2}/{c^2}+1\right)\left(1-{a^2}/{b^2}\right)} \qquad (79)$$

Therefore, from the Lamé solution for a single hollow cylinder, the solution for radial stress for the condition $a \le r \le b$ is

$$\sigma_r = \frac{1}{1-{a^2}/{b^2}}\left[\left(P_i\,{a^2}/{b^2} - P_b\right) - (P_i - P_b)\,{a^2}/{r^2}\right] \qquad (80)$$

where, P_b is given in (79).

The tangential stress σ_θ is simply the conjugate of (80). As for the stress distribution for $b \le r \le c$, this is simply the Lamé solution for *inner* pressure, P_i, equal to the boundary pressure, P_b, and outer pressure P_o, the same as before. The inner radius becomes b and the outer radius is c.

It is straight forward to check the boundary pressure, P_b, for the case of a cylinder inside a circular hole in an infinite plate. This problem implies, the outermost radius c extends to infinity and the external pressure P_o is zero. Therefore,

$$P_b = \frac{2P_i \, a^2/b^2 \, (1-\upsilon_1) G_2}{G_2\left((1-2\upsilon_1) + a^2/b^2\right) + G_1\left(1 - a^2/b^2\right)}$$

$$P_b = \frac{2P_i \, a^2/b^2 \, (1-\upsilon_1)}{2(1-\upsilon_1) + \left(G_1/G_2 - 1\right)\left(1 - a^2/b^2\right)} \tag{81}$$

(81) is consistent with the result for an internally pressurized annulus in an infinite plate (Crouch & Starfield, 1983).

The urethane packer used in all experiments is essentially a hollow cylinder inside a borehole and the radial and tangential stresses are evaluated from (80) and (81). The stresses acting on the boundary between the urethane and specimen will be *proportional* to the internal pressure, not directly equal to it. If the shear moduli, $G_2 >> G_1$ (Figure 22) such as the case when the urethane packer is inside a much stiffer hollow cylinder, then (81) reduces to

$$P_b = \frac{2P_i \, a^2/b^2 \, (1-\upsilon_1)}{(1-2\upsilon_1) + a^2/b^2} \tag{82}$$

The ratio, P_b/P_i was estimated for the urethane packer with properties shown in Table 1.

Table 1: Properties of urethane packer

Inner radius, a	Outer radius, b	Poisson's ratio, ν_1	Shear modulus, G_1
[mm]	[mm]		[MPa]
5.5±0.1	9.7±0.1	0.47±0.3	33±2.0

$$\frac{P_b}{P_i} = 0.893 \tag{83}$$

However, since the Poisson's ratio of the rubber packer is not well known, a simple calibration procedure was used to determine the ratio P_b/P_i.

The calibration procedure involved a hollow T6061 aluminum cylinder (material properties in Table 2) with three lateral strain gages glued to the outer surface of the cylinder (Figure 23). The urethane packer was inserted into the aluminum cylinder and pressurized with water at an approximate rate of 1.2 cc/min.

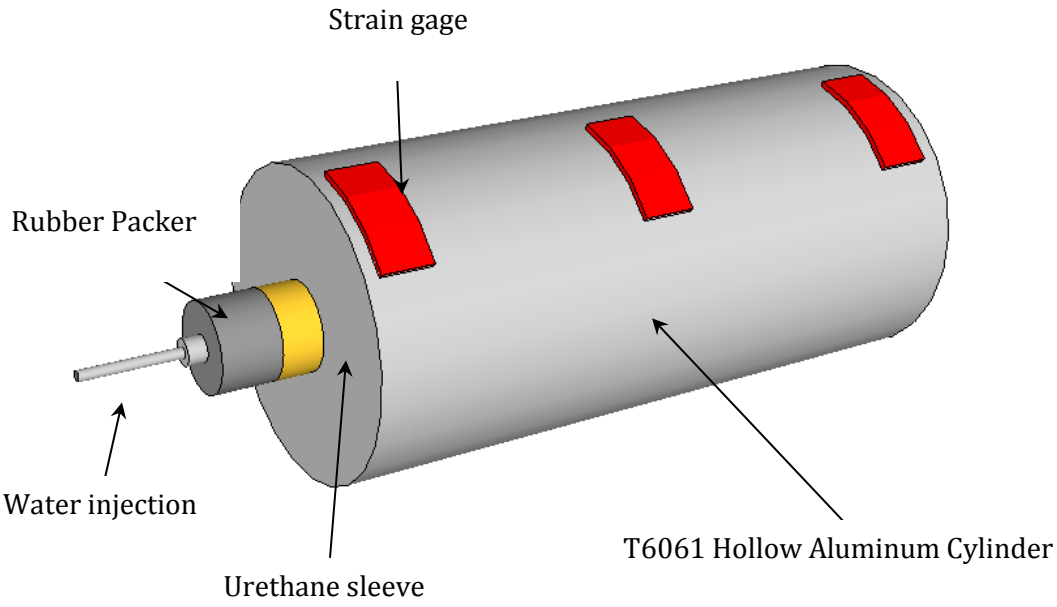

Figure 23: Hollow Aluminum Cylinder with urethane packer

Table 2: Measured properties of hollow aluminum cylinder

Young's modulus, *E*	Poisson's ratio, ν	Shear modulus, G
[GPa]		[GPa]
71.4 ± 3.5	0.343 ±0.02	26.6 ± 1.3

The strain gages on the surface of the aluminum cylinder were Vishay 120Ω general purpose strain gages that measured tangential strain along the surface. Since the aluminum cylinder can be considered isotropic and linearly elastic, the stress-strain relationship at the boundary is given according to Hooke's Law:

$$\varepsilon_\theta = \frac{1}{E}(\sigma_\theta - \upsilon\sigma_r) \tag{84}$$

At the outer boundary $r = b$, the radial stress is zero and (84) reduces to

$$\varepsilon_\theta = \frac{\sigma_\theta}{E} \tag{85}$$

From the Lamé solution for an internally pressurized cylinder, the tangential stress, σ_θ, at the boundary $r = b$ is

$$\sigma_\theta = \frac{2P_b a^2}{b^2 - a^2} \tag{86}$$

The radial stress σ_r is, of course, zero.

From (85) and (86), the boundary pressure P_b is,

$$P_b = \frac{E\varepsilon_\theta(b^2 - a^2)}{2a^2} \tag{87}$$

Because of the presence of the urethane sleeve inside the hollow aluminum cylinder the boundary pressure, P_b, will be reduced from the internal pressure P_i by a constant, C (note $C < 1$).

$$\frac{P_b}{P_i} = C = \frac{E\varepsilon_\theta(b^2 - a^2)}{P_i 2a^2} \tag{88}$$

Therefore, from (88), $1/C$ is equal to the slope of the curve on the normalized internal pressure, P_i/E, versus tangential strain, ε_θ^*, where

$$\varepsilon_\theta^* = \frac{\varepsilon_\theta(b^2 - a^2)}{a^2} \tag{89}$$

The calibration constant C for the case of the urethane packer and hollow aluminum cylinder with properties given in Table 1 is shown in Figure 24.

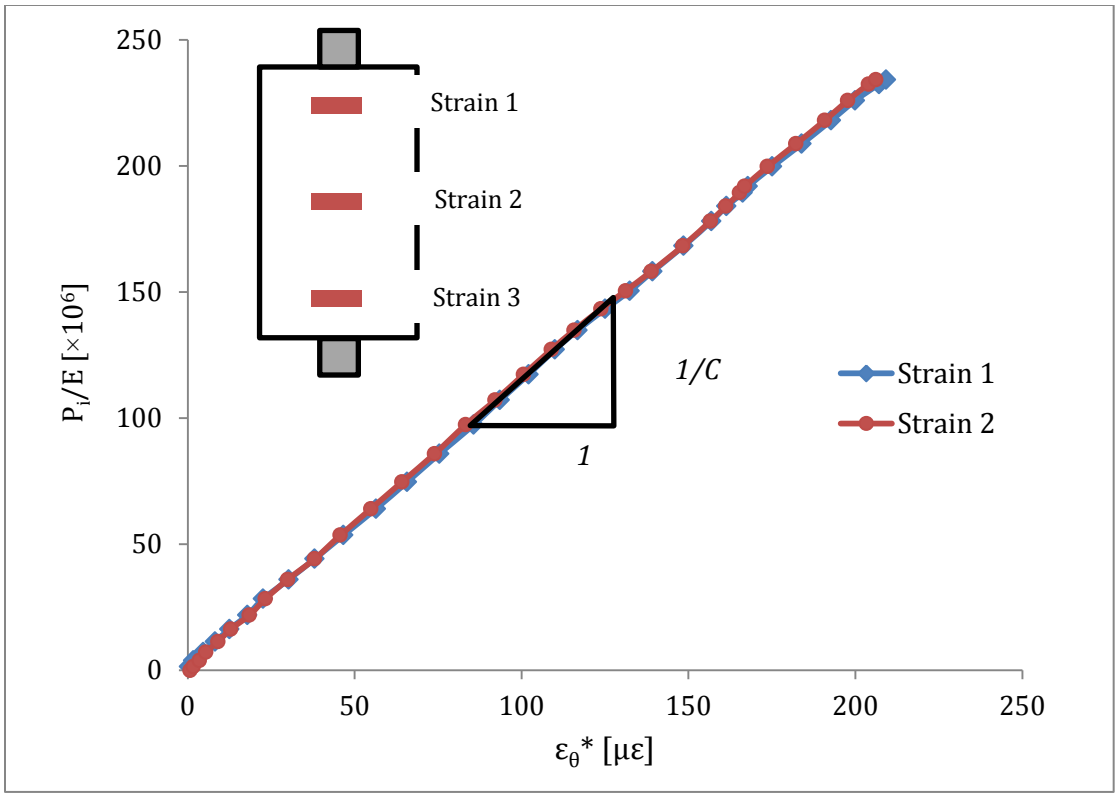

Figure 24: Plot showing normalized internal pressure versus tangential strain for determining calibration constant C. Figure in upper left corner shows the locations of the strain gages glued to aluminum cylinder.

$$\frac{1}{C} \approx 1.1238 \rightarrow C \approx 0.890$$

Comparing the calibration constant C to the result from (83) yields a percent difference of 0.34%. Therefore, the urethane packer is calibrated accurately.

3.4 Specimen Preparation

Specimens were precision ground to cubic dimensions: 100mm × 100mm × 100mm in size. Each surface was machined parallel to the opposite face and orthogonal to the adjacent face. The tolerance for the laterally loaded surfaces was allowed to be ±0.5 mm due to the expansion of the flat-jacks. The tolerance of the surface loaded by the ALC had to maintain a minimum of 100mm to allow clearance for the lateral platens. A center hole was cored with a 20mm diameter diamond coring bit to produce the borehole. After surface grinding and cutting the center hole the specimen was placed in an oven at 70° C to dry for 24 hrs.

The rocks tested were Indiana limestone and Berea sandstone. Indiana limestone is calcareous stone, lightly bedded with grain size on the order of 1mm. The tested Indiana limestone had the following properties: shear modulus = 7.3 – 8.0 GPa, density = 2.23 g/cm^3, tensile strength = 7.4 - 8.4 MPa. The shear modulus and tensile strength were based on cavity expansion experiments outlined in section 4.1. Berea sandstone is thinly bedded, light-gray, medium to fine grained sandstone with grain sizes of 0.1 to 0.8 mm. Berea sandstone's constituent minerals are 78% quartz and 16% feldspar (Krech *et al.* 1974). The tested Berea sandstone had the following properties: shear modulus, G = 3.8 – 5.6 GPa, density ρ = 2.11 g/cm^3, tensile strength = 4.0 - 5.6 MPa.

3.5 Testing Procedure

Once the specimen was properly dried, a base primer coat was applied to the surface that was monitored. The base primer requires 4hrs to dry. Two coats of primer were applied after drying. Once the primer was dried, a flat white paint was brushed on the surface. Any rough edges that develop from the paint were sanded down with 400 grit sandpaper. Two coats of paint were added to the surface. The primer and paint made for an overall thickness of approximately 15 μm (Kao, 2011). Throughout the application process, the dry surface was intermittently sprayed with a pressurized air hose to eject any stray particles. Once the white paint was completely dry, the speckle pattern was produced by spraying the surface with a flat-black aerosol spray can. The speckle pattern produced optimal displacement resolution when the speckles were distributed evenly with no significant clustering.

After the paint had completely dried, a stearic acid mixture was applied to each surface of the specimen that was in contact with a loading platen. The stearic acid mixture (Labuz & Bridell, 1993) significantly reduces stress concentration at the contact of the platen and specimen. Stearic acid was also applied to the painted surface and heated to create a transparent layer on the surface.

Once the specimen was prepared, it was placed in the CEA with the urethane packer inserted into the borehole. Depending on the chosen loading configuration, the CEA was assembled as described in section 4.1. Data acquisition was set at 1 Hz for both the DIC camera and borehole pressure monitoring. Along with borehole pressure data, the volume change in the packer was recorded throughout the test. Synchronized time was important to properly correlate DIC images with borehole pressure values, so both data acquisition systems were started at the same running time.

Chapter 4

Results

4.1 Measurement of Shear Modulus

The shear modulus, *G*, was measured for both Berea sandstone and Indiana limestone specimens. Values for the shear modulus were measured by uniformly pressurizing the circular cavity and monitoring surface displacements. No additional far-field stresses were applied. The internal pressure as a function of volume change is shown in Figure 25.

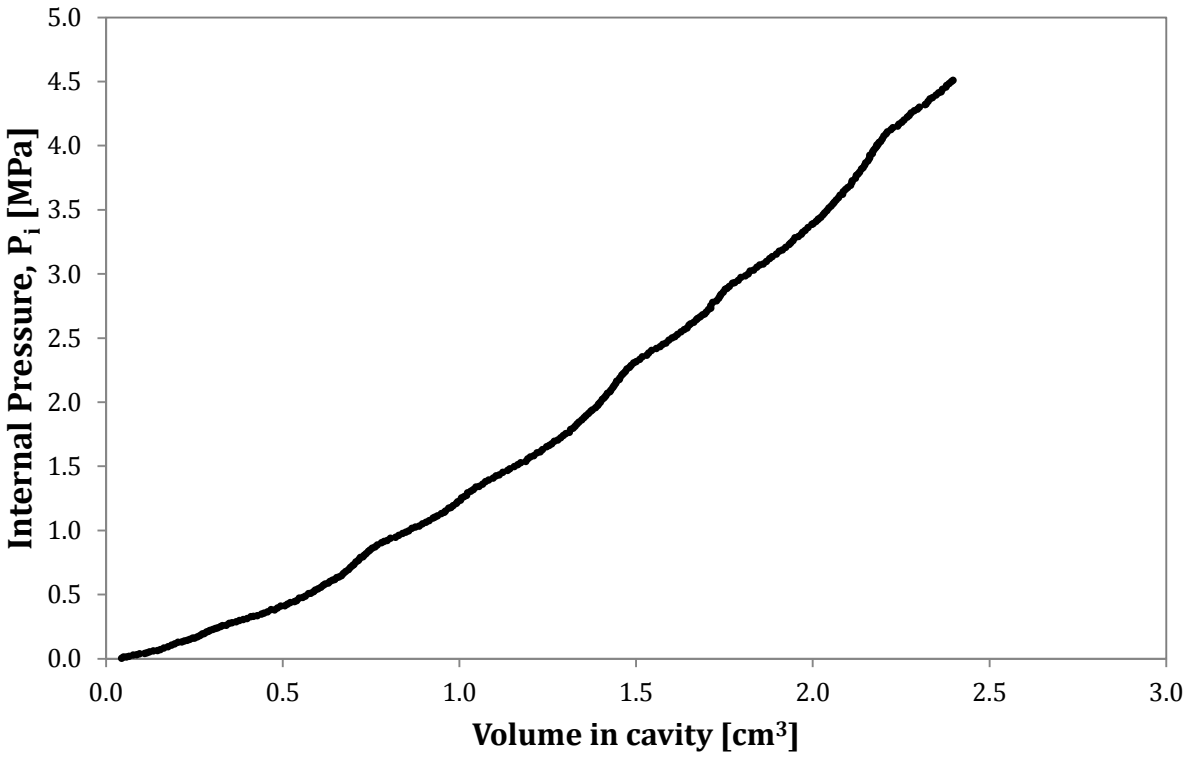

Figure 25: Loading plot of internal pressure versus volume for Berea sandstone.

The *incremental* radial displacement contours for a Berea specimen pressurized from *1 – 4.5MPa* are shown in Figure 26.

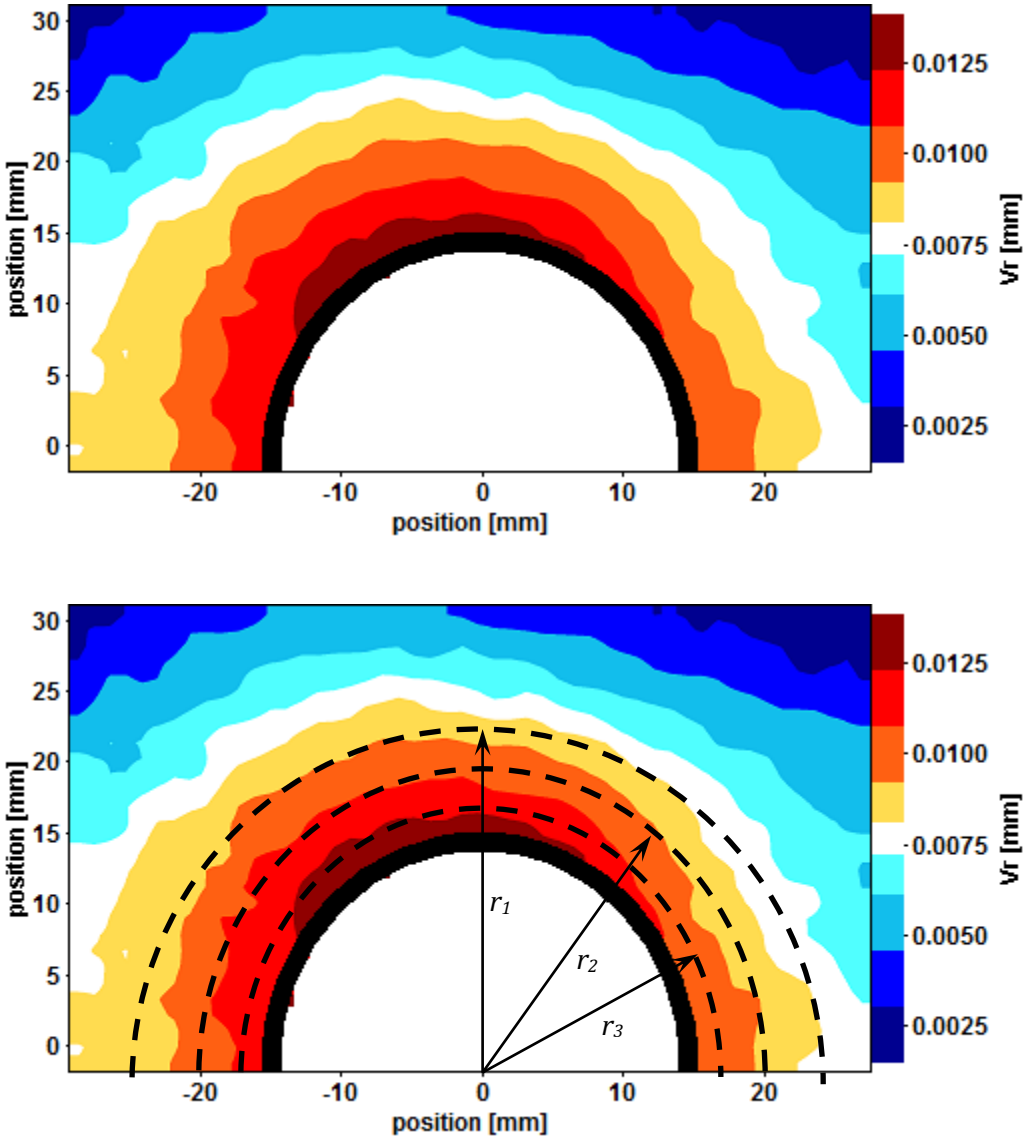

Figure 26: (Top) Radial displacement contours for Berea sandstone internally pressurized from 1MPa to 4.5MPa. (Bottom) Radial displacement evaluated at the three different radii.

The shear modulus was computed from the average radial displacement u_r in Figure 26 for radii equal to 15mm, 20mm and 25mm. From (34):

$$\Delta P_i \frac{a}{r} = 2G \frac{\Delta u_r}{a} \tag{90}$$

Figure 27 shows a plot for the Berea sandstone specimen in Figure 26, where the shear modulus is proportional to the slope, *m*.

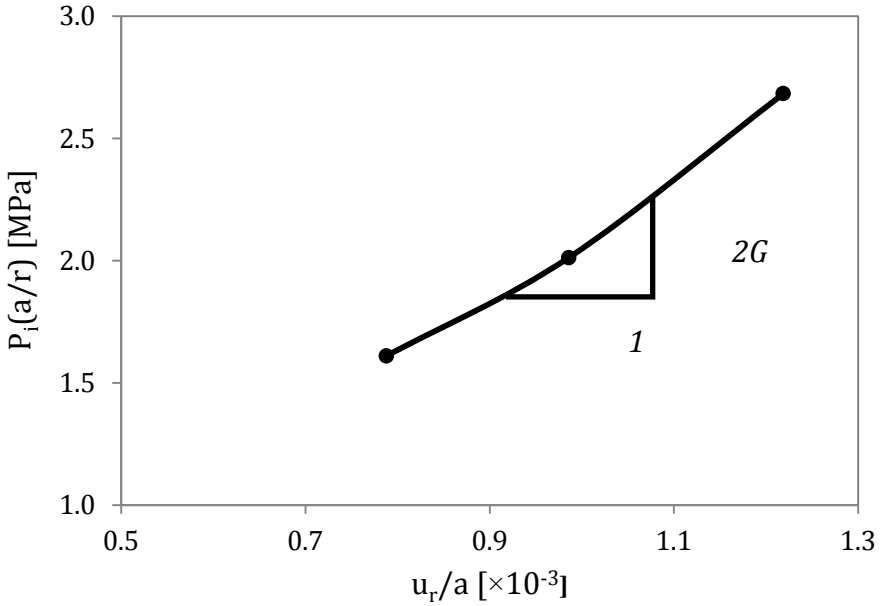

Figure 27: Determination of the shear modulus for a Berea sandstone specimen.

The increment of internal pressure was *3.5MPa* and the slope *m* from Figure 27 was 2.5, therefore:

$$G = \frac{m}{2} \approx 1.3\ GPa$$

The shear modulus for different specimens is shown in Table 3, along with the measured value of tensile strength.

Table 3: Material parameters from cavity expansion experiment

Specimen	Shear Modulus, G	Tensile Strength
[]	[GPa]	[MPa]
CE_S1	1.3	5.6
CE_S2	2.3	4.0
CE_S3	1.2	4.2
CE_S4	1.5	5.0
CE_L1	9.3	7.4
CE_L2	8.0	8.4
CE_L3	8.7	7.8
UC_L1*	11-12	-

*Measured from Uniaxial Compression (UC) tests (Makhnenko & Labuz, 2013)

4.2 Fracture Properties

Analysis of the displacement field using DIC allowed tracking the development of a fracture prior to peak pressure. Fracture characteristics were compared to DIC measurements from three-point-bending (3PB) experiments on the same rock.

Figure 28 shows the horizontal displacement contours for an interval of *20-70%* peak pressure. The horizontal contours show displacement left of the center line to the left and displacement right of the center line to the right. The color indicates magnitude of horizontal displacement. The center of the cavity is located at point *(0,0)* with radius *a.* The fracture will begin to develop at the boundary where $\theta \approx 90°$.

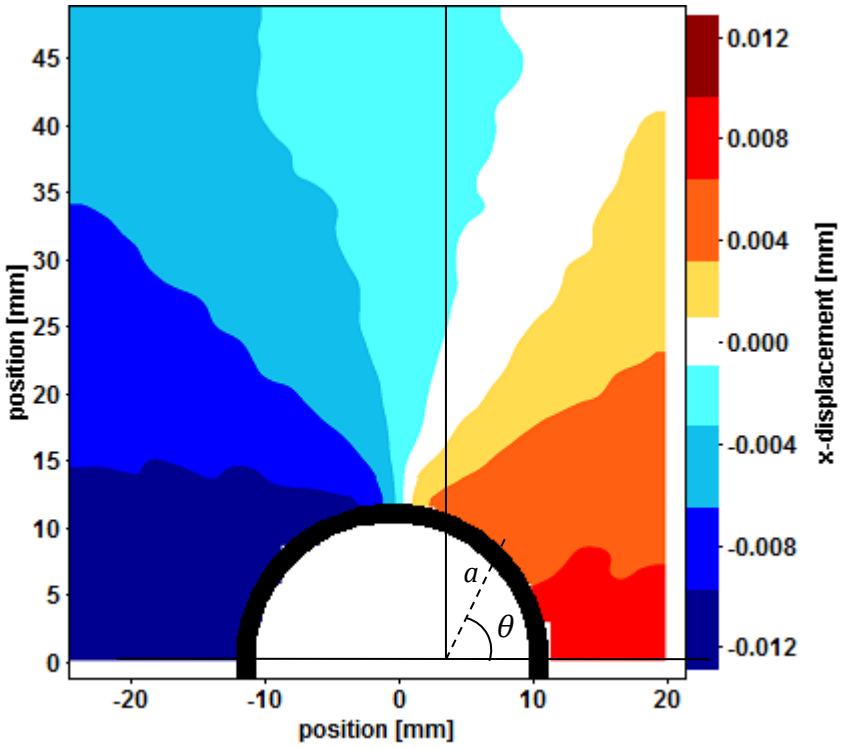

Figure 28: Horizontal displacement contours for a Berea specimen 20-70% peak pressure.

The development of a fracture at the cavity boundary prior to peak pressure was observed in all tested specimens. Lin and Labuz (2013) showed that in three-point-bending

experiments, the tip of the fracture process zone (FPZ) can be identified by the location where the horizontal displacement contours merge. The same concept was used to track the development of the fracture in the cavity expansion experiments.

Once the internal pressure increases in the cavity to a certain amount, a damage zone begins to form. As the internal pressure is further increased, the damage zone develops and the tip can be identified where the contours merge. Figure 29 shows the incremental horizontal displacement contours for *80-90%* peak pressure. The tip of the "fracture" is located at $y \approx 15mm$.

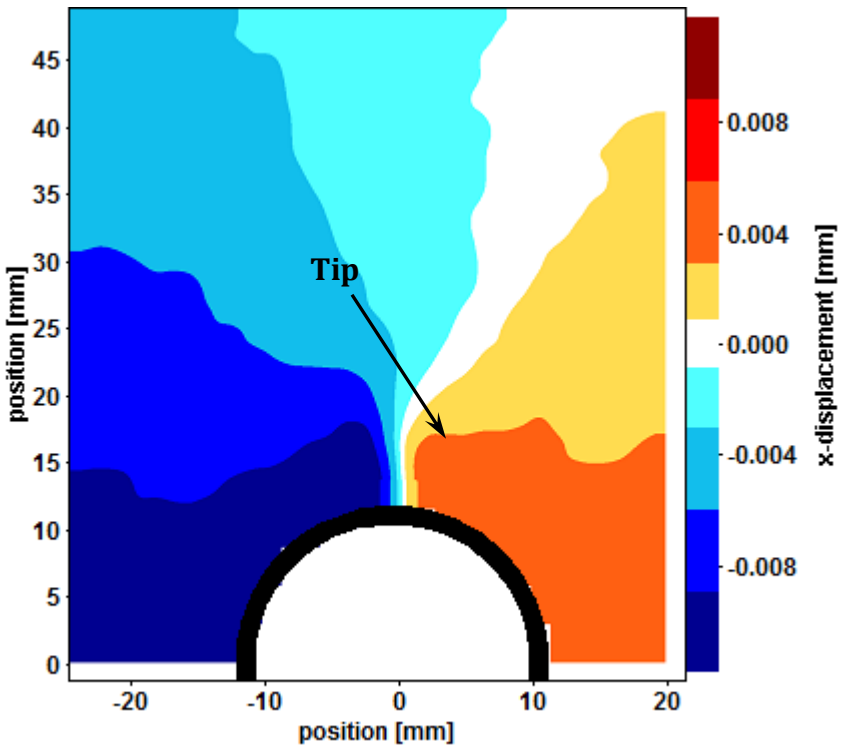

Figure 29: Incremental horizontal displacement contours for 80-90% peak pressure.

The initial formation of a traction free surface is assumed to be indicated by the critical crack opening displacement (CCOD), w_c. It is the measure of the total opening displacement from initiation to peak load from chosen points on both sides of the crack and is often

considered to be a material parameter. The points of measurement are usually located 1-2mm on each side of the crack because measurement at exactly the crack face is not possible with DIC. In the cavity expansion experiments, a traction free surface was assumed to have developed at peak internal pressure. From the location of the crack tip an effective crack length L_{eff} was measured. The effective crack length included the radius of the hole and the length from the boundary to where the contours merged.

Indiana Limestone

The same analysis was performed on Indiana limestone. The cavity was pressurized using a selected distribution of tractions (see section 3.1). For the specimen in Figure 30, initiation was first observed to occur between 50-60% peak pressure.

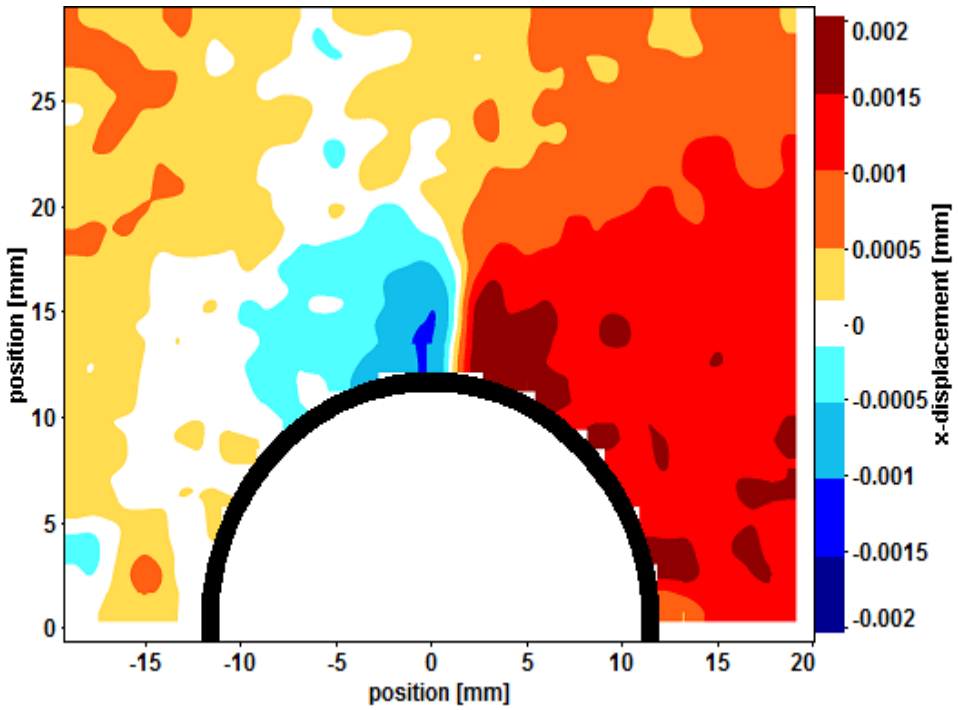

Figure 30: Incremental horizontal displacement contours for an Indiana limestone specimen (CE_L13) from 50-60% peak pressure

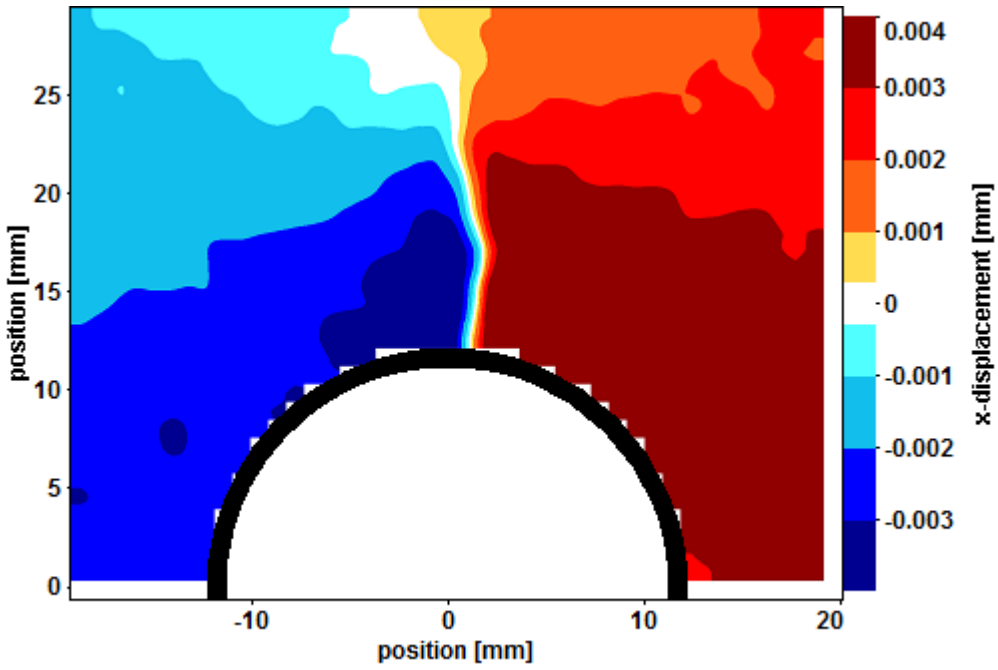

Figure 31: Incremental horizontal displacement contours for an Indiana limestone specimen (CE_L13) from 50-80% peak pressure

Figure 32 and 33 show the incremental horizontal displacement contours at 100% peak pressure for two different Indiana limestone specimens. The tip of the fracture is beyond the field of view and cannot be measured. However, from the total displacement profile the CCOD was measured as *24mm* in Figure 32 and *20mm* in Figure 33.

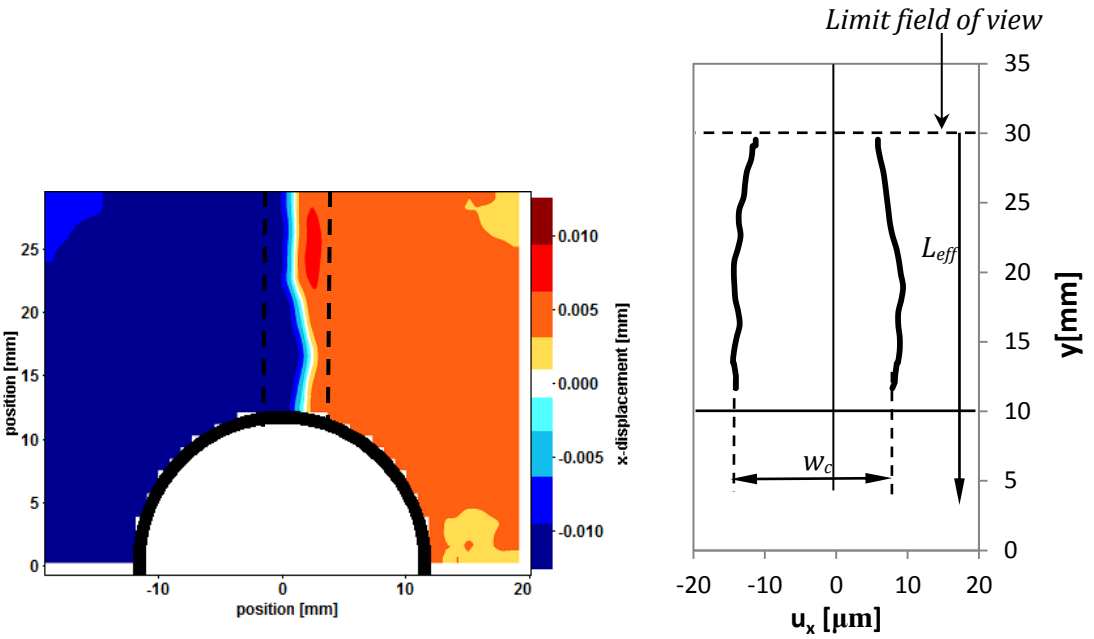

Figure 32: (Left) Incremental horizontal displacement contours for an Indiana limestone specimen (CE_L13) from 80-100% peak pressure (Right) Total horizontal displacement measurements from 60-100% peak pressure along vertical lines at x = -0.9mm (left line) and x = 2.7mm (right line)

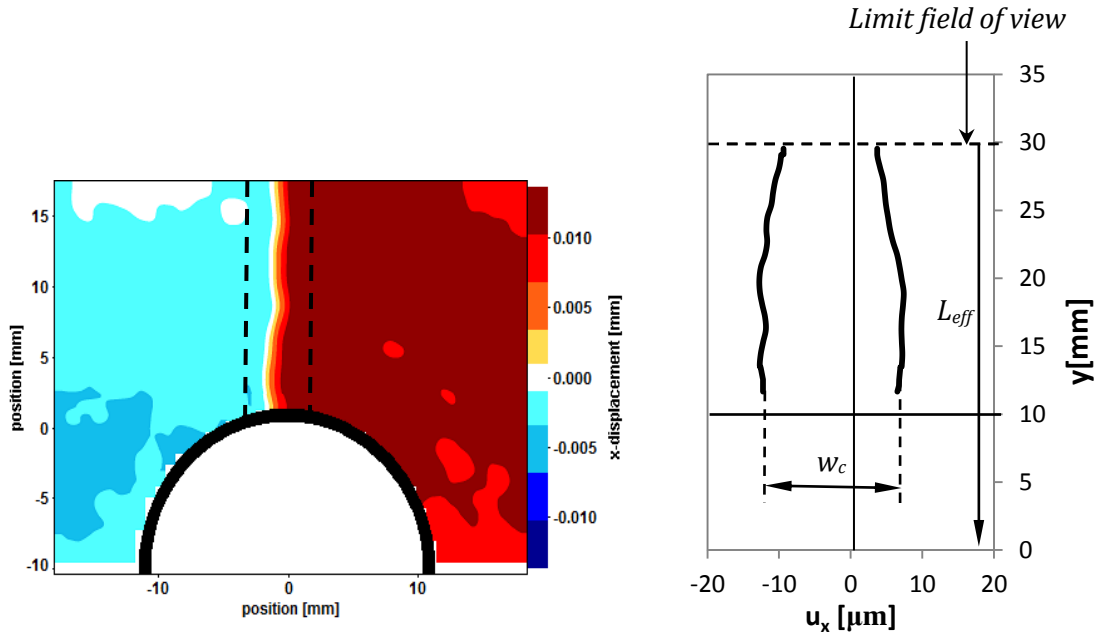

Figure 33: (Left) Incremental horizontal displacement contours for an Indiana limestone specimen (CE_L7) from 90-100% peak pressure (Right) Total horizontal displacement measurements from 60-100% peak pressure along vertical lines at x = -2.3mm (left line) and x = 0.3mm (right line)

From 3PB experiments on Indiana limestone, the critical crack opening displacement was measured as *16μm* and the effective crack length at peak load was *16mm*. Figure 34 and 35 show the horizontal displacement contours from 60-100% peak load and the total horizontal displacement profile from 60-100% peak load for two different specimens.

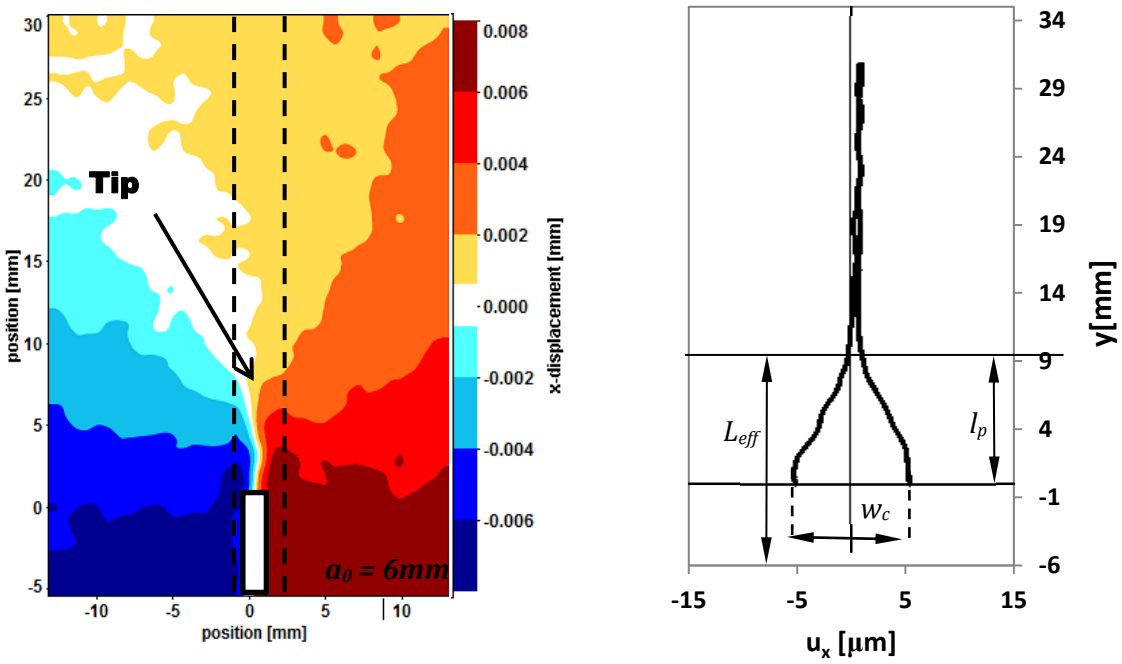

Figure 34: (Left) Incremental horizontal displacement contours for a large-size specimen (3PB_L1) from 95% -100% peak. (Right) Total horizontal displacement measurements from 60% - 100% peak along vertical lines at x = -0.8mm (left line) and x = 2mm (right line)

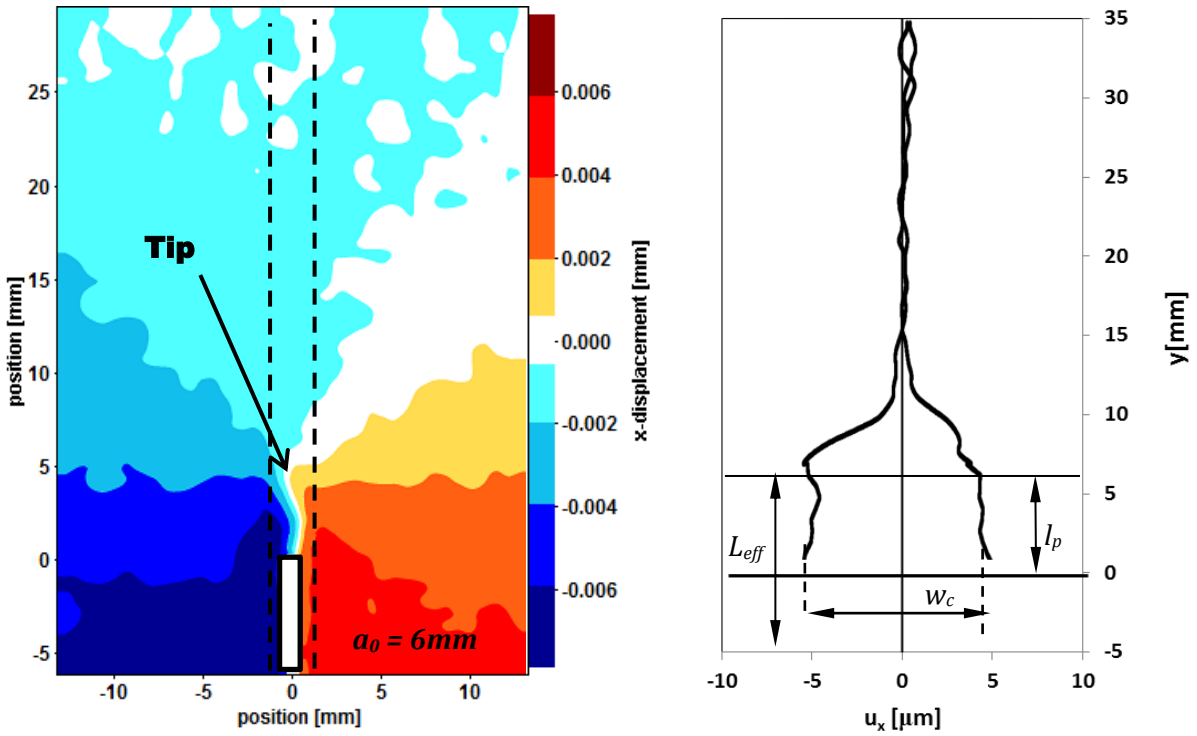

Figure 35: (Left) Incremental horizontal displacement contours for a large-size specimen (3PB_L2) from 90% - 100% peak. (Right) Total horizontal displacement measurements from 60% - 100% peak along vertical lines at x = -1mm (left line) and x = 1mm (right line)

Table 4 shows the fracture properties for Indiana limestone specimens from cavity expansion and three-point-bend experiments.

Table 4: Fracture properties for Indiana limestone specimens from CE and 3PB experiments.

Specimen	Initiation	CCOD, w_c	Effective Crack Length , L_{eff}
[]	[% Peak*]	[mm]	[mm]
CE_L7	60	20	>20
CE_L13	60	24	>20
3PB_L1	60	16	16
3PB_L2	60	14	15

* Peak pressure and peak load for CE and 3PB experiments respectively

Berea Sandstone

The Berea sandstone specimen shown in Figure 36 was pressurized using a selected distribution of tractions (see section 3.1). Initiation was first observed to occur between incremental loadings of 70-80% peak pressure. Therefore, it can be estimated that the fracture begins to form at 80% peak pressure. Increments of loading smaller than 10% proved difficult to identify where the contours merged.

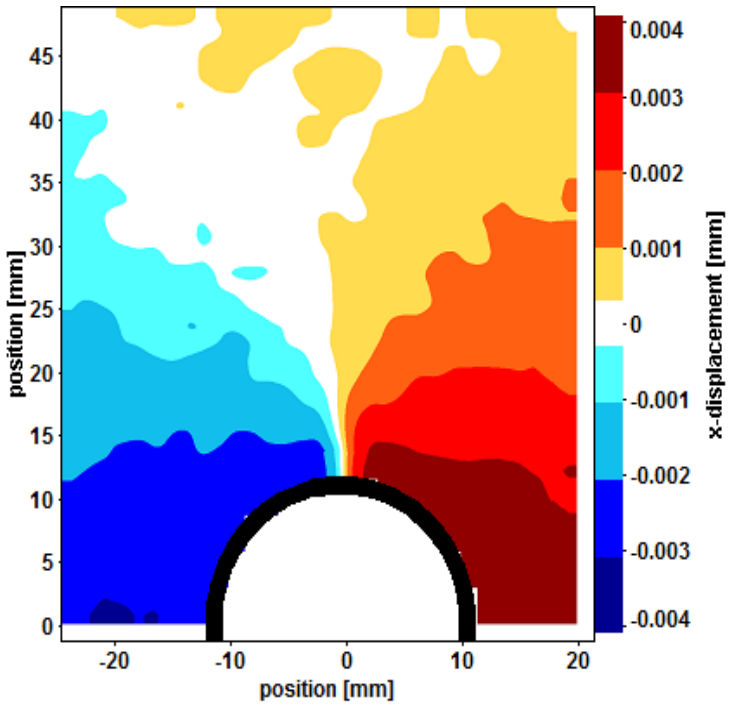

Figure 36: Incremental horizontal displacement contours for a Berea sandstone (CE_S5) from 70-80% peak pressure

Figure 37 shows the development of fracture from 80-95% incremental pressure. The tip is now located at approximately *y=20mm*.

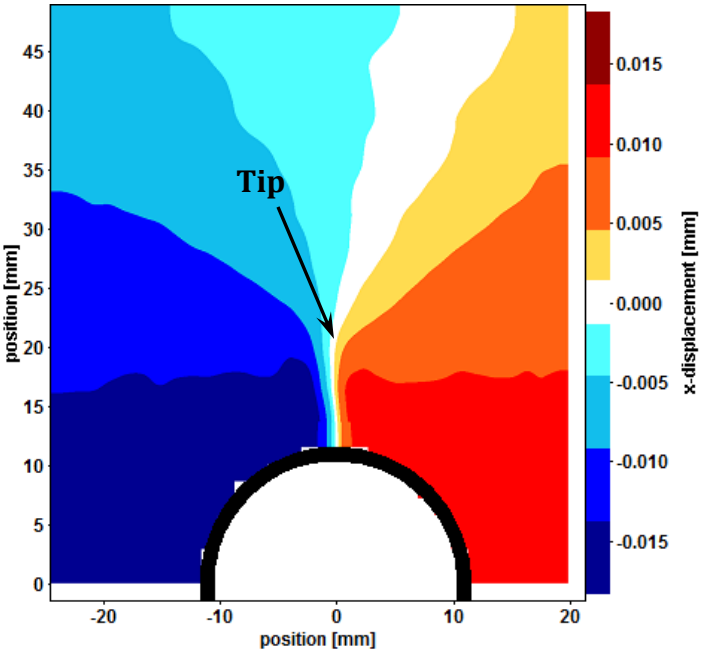

Figure 37: Incremental horizontal displacement contours for a Berea sandstone (CE_S5) from 80-50% peak pressure

Figure 38 shows the horizontal displacement measurements from 90-100% peak pressure. From this figure, the tip of the fracture is estimated to be at $y \approx 30mm$. The figure on the right shows *total* horizontal displacement (80-100% peak pressure) versus *y-position* along two vertical lines located at $x = -1.5mm$ and $x = 1.7mm$. The crack opening displacement, w, is the distance between the two curves at the hole radius ($y = 10mm$), for this Berea specimen, w_c = 68µm. The effective crack length L_{eff} was *30mm*.

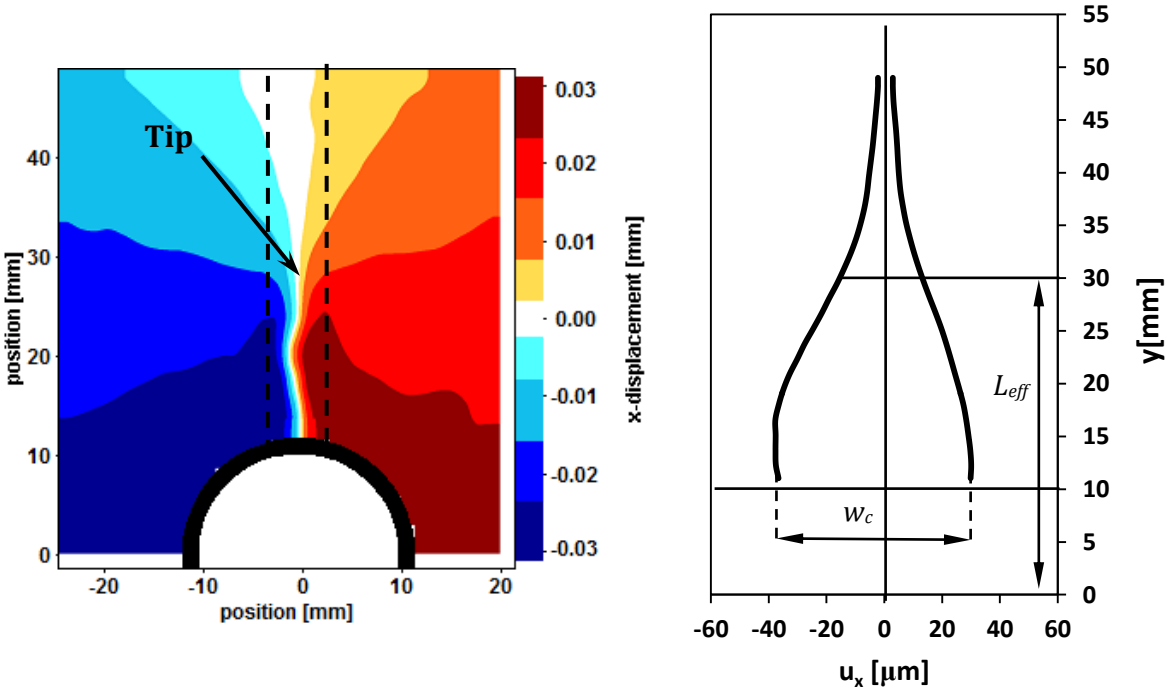

Figure 38: (Right) Incremental horizontal displacement contours for a Berea specimen (CE_S5) from 90-100% peak pressure (Left) Total horizontal displacement measurements from 80-100% peak pressure along vertical lines at x = -1.5mm (left line) and x = 1.7mm (right line)

The same analysis for Indiana limestone was performed on Berea sandstone where the surface being monitored had normal traction applied to the surface to keep the out of plane displacement zero (biaxial strain). This condition required using a glass plate in contact with the specimen to view displacements. The field of view was limited to a 30mm × 30mm window. The cavity was subjected to uniform pressure and a far-field normal stress was applied in one direction to allow the fracture plane to propagate parallel to the direction of the far-field stress. Initiation was measured at 70-80% peak pressure.

Figure 39 and 40 show horizontal displacement contours from 95-100% peak pressure as well as the total horizontal profile from 80-100% peak pressure. From these figures, the tip of the fracture is beyond the field of view and cannot be measured. However, from the

total displacement profile the critical crack opening displacement was 90μm for the specimen in Figure 39 and 57μm for the specimen in Figure 40.

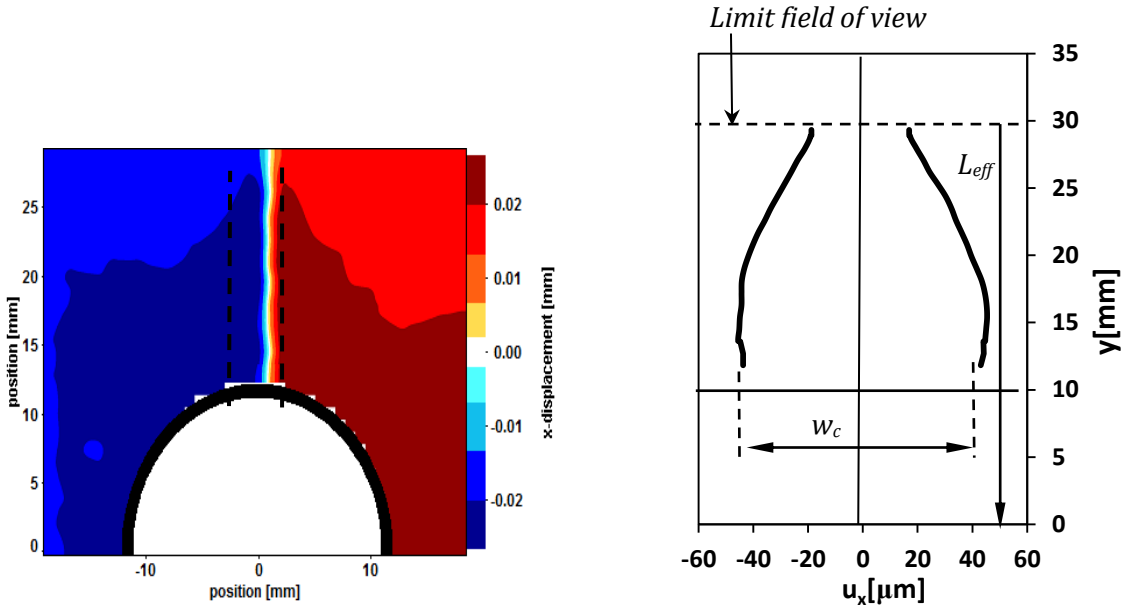

Figure 39: (Left) Incremental horizontal displacement contours for a Berea specimen (CE_S3) from 95-100% peak pressure (Right) Total horizontal displacement measurements from 80-100% peak pressure along vertical lines at x = -0.9mm (left line) and x = 2.7mm (right line)

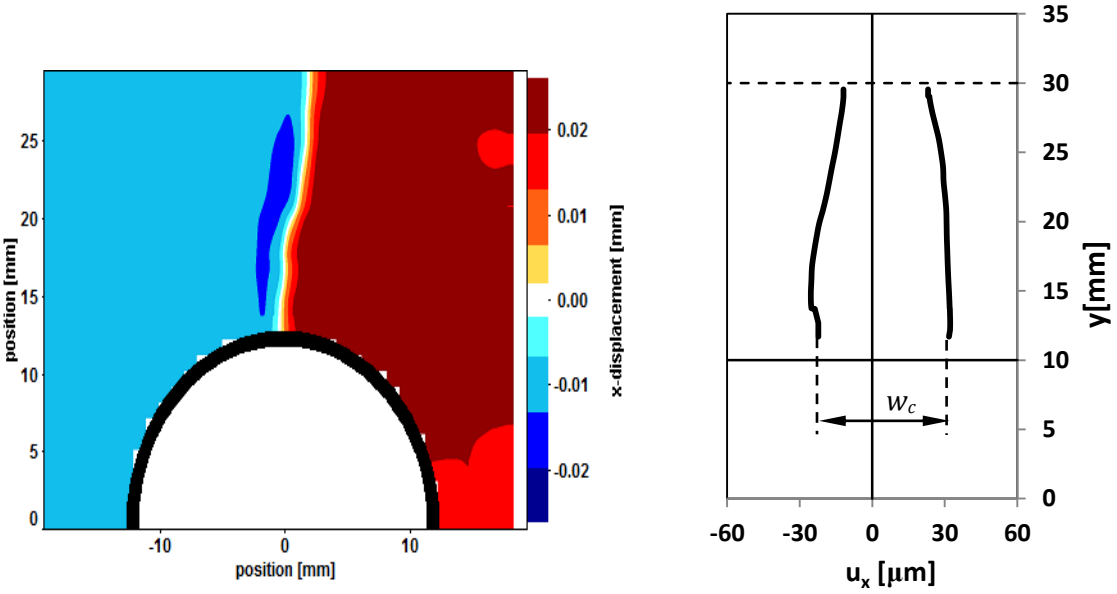

Figure 40: (Left) Incremental horizontal displacement contours for a Berea specimen (CE_S2) from 90-100% peak pressure (Right) Total horizontal displacement measurements from 80-100% peak pressure along vertical lines at x = -0.9mm (left line) and x = 2.7mm (right line)

Three-point-bending tests on the Berea sandstone were analyzed in the same way as for the cavity expansion tests. However, the effective crack length, L_{eff}, includes the length of the notch ($a_o = 0.2*D$) and the length measured from the notch tip to the location where the contours merge (length of FPZ). Figure 41 and 35 show the horizontal displacement contours for beam specimens subjected to three-point-bend loading conditions.

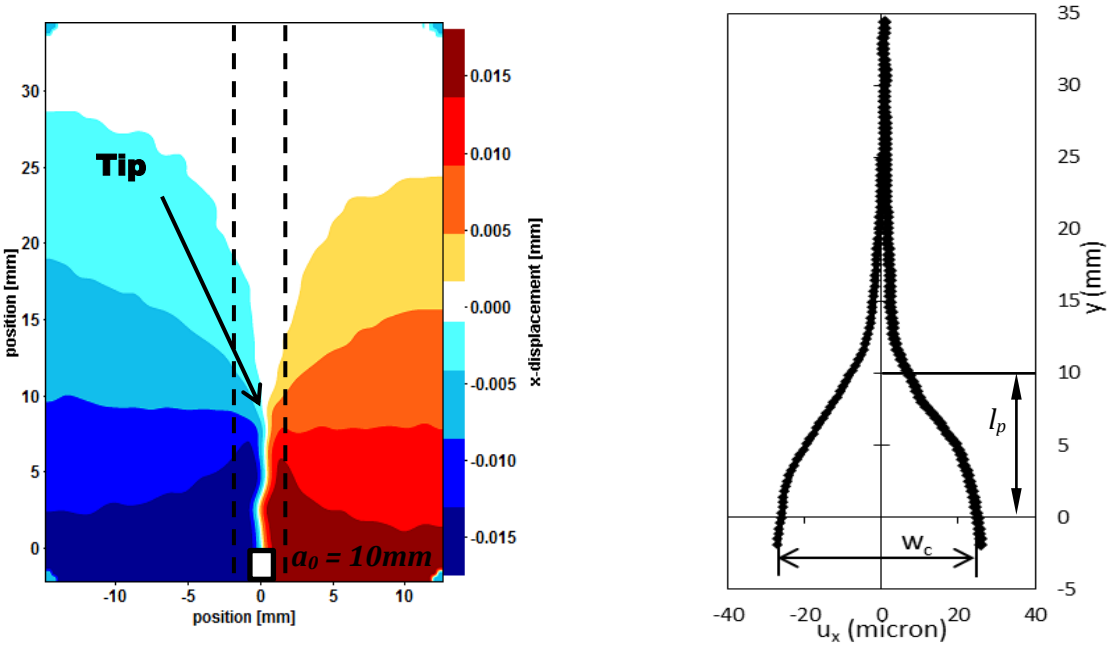

Figure 41: (Left) Incremental horizontal displacement contours for a Berea specimen (3PB_S1) from 90-100% peak load (Right). Total horizontal displacement measurements along vertical lines at x = -1.6mm) and x = 1.7mm – Manning (2012)

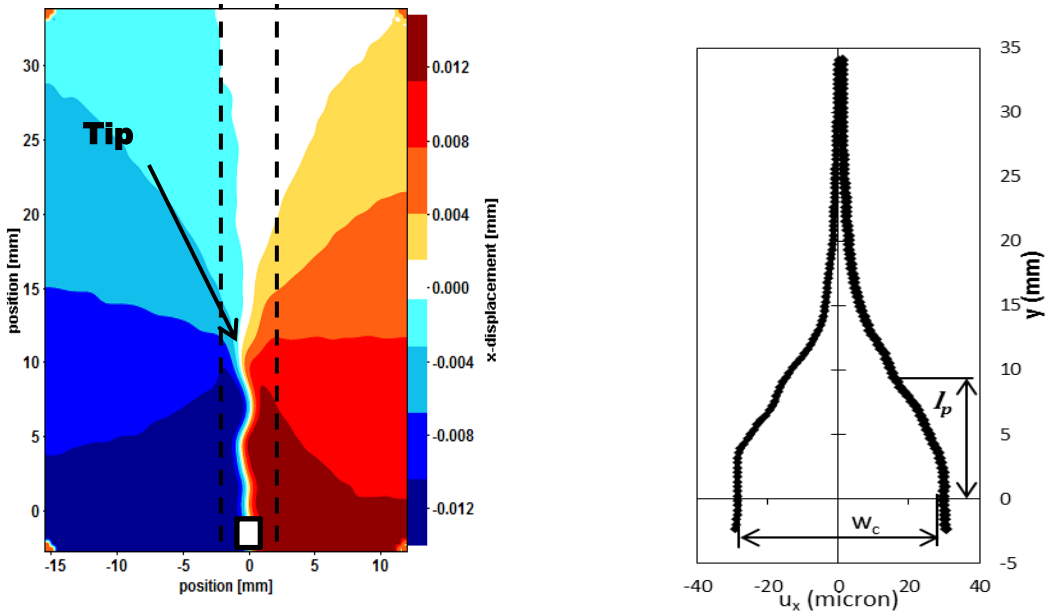

Figure 42: (Left) Incremental horizontal displacement contours for a Berea specimen (3PB_S2) from 95-100% peak (Right) Total horizontal displacement measurements from 70-100% peak along vertical lines at x = -1.8mm and x = 1.5mm – Manning (2012).

Table 5 shows fracture measurements for Berea sandstone specimens from cavity expansion tests and three-point-bend experiments.

Table 5: Fracture properties for Berea sandstone specimens from CE and 3PB experiments.

Specimen	Initiation	CCOD, w_c	Effective Crack Length , L_{eff}
[]	[% Peak*]	[mm]	[mm]
CE_S2	70	57	>20
CE_S3	80	90	>20
CE_S5	80	68	30
3PB_S1†	70	51	20
3PB_S2†	70	58	27

* Peak pressure and peak load for CE and 3PB experiments respectively
† Three-point-bending tests from Manning (2012)

Chapter 6

Conclusions

Fracture near a pressurized circular cavity in rock is critical for several important processes, yet few observations exist. However, with the application of the cavity expansion apparatus (CEA), direct measurement of fracture properties was achieved using the digital image correlation (DIC) technique. In addition the CEA, also provided an effective way of controlling where the fracture would initiate and thus made it possible to observe fracture initiation.

The cavity expansion apparatus provided insight on the development of a fracture near a circular hole and gave convincing evidence that a discontinuity in the displacement field is formed prior to peak internal pressure. It was found that a "fracture" developed at 80% and 60% peak internal pressure for Berea sandstone and Indiana limestone respectively. Further characterizing the fracture was achieved by assuming that the critical crack opening displacement (CCOD) signifies the start of unstable crack growth. From this assumption, it was found for cavity expansion experiments that the CCOD was 57μm-90μm and 20μm-24μm for Berea sandstone and Indiana limestone respectively. From three-point-bending experiments, the CCOD was 51μm-58μm and 15μm-16μm for Berea sandstone and Indiana limestone respectively. On average, the CCOD was 35% higher in cavity expansion experiments than three-point-bend experiments for Berea sandstone and 42% higher for Indiana limestone, suggesting stable growth prior to peak pressure.

Future work on this subject is open to a number of possibilities. One application would be modifying the CEA to accommodate fluid infiltration into the specimen. This would provide

a unique insight on the development of a hydraulic fracture that includes internal cavity pressure as well as normal tractions acting directly on the crack surface. Analyses for this type of loading have been developed, however little direct experimental verification has been performed.

References

Abou-Sayed, A. S. (1977). Fracture Toughness, K_{Ic}, of Triaxially-Loaded Indiana Limestone. *Proc. 18th Symp. Rock Mech.*

Amadei, B., & Stephansson, O. (1997). *Rock Stress and its Measurement.* London and New York: Chapman & Hall.

Barrenblatt, G. I. (1959). The formation of equilibrium crack during brittle fracture - general ideas and hypothesis. *Journal of Applied Mathematics and Mechanics*, 434-44.

Bazant, Z. P., & Planas, J. (1998). *Fracture and size effect in concrete and other quasibrittle materials.* CRC Press.

Beuckner, H. F. (1960). Some stress singularities and their computation by means of integral equations. *Boundary Problems in Differential Equations*, 215-30.

Bowie, O. L. (1956). Analysis of an infinite plate containing radial cracks originating at the boundary of an internal circular hole. *J. Math. Phys.*, 60-71.

Bowie, O. L. (1964). Rectangular Tensile Sheet with Symmetric Edge Cracks. *Transactions of the ASME*, 208-212.

Bowie, O. L., & Freese, C. E. (1972). Elastic Analysis for a Radial Crack in a Circular Ring. *Eng. Fract. Mech.*, 315-21.

Bray, J. (1987). Some Applications of Elastic Theory. In E. T. Brown, *Analytical and Computational Methods in Engineering Rock Meachanics* (pp. 32-94). London: Allen & Unwin.

Bruck, H. A., McNeill, S. R., Sutton, M. A., & Peters, W. H. (1989). Digital Image Correlation Using Newton-Raphson Method of Partial Differential Correction. *Experimental Mechanics*, Volume 29. Issue 3. 261-67.

Chen, D. J., Chiang, Y. S., Tan, & Don, D. S. (1993). Digital Speckle-Displacement Measurement Using a Complex Specturm Method. *Applied Optics*, Vol. 32, Issue 11. 1839-49.

Clifton, R. J., Simonson, E. R., Jones, A. H., & Green, S. J. (1976). Determination of the Critical-stress-intensity Factor, KIc from Internally Pressurized Thick-walled Vessels. *Experimental Mechanics*, 233-38.

Crouch, S. L., & Starfield, A. M. (1983). *Bounday Element Methods in Solid Mechanics.* London: George & Unwin.

Dugdale, D. W. (1960). Yielding of steel sheets containing slits. *Jounrnal of the Mechanics and Physics of Solids*, 59-68.

Griffith, A. A. (1920). The phenomena of flow and rupture in solids. *Phil. Trans. Roy. Soc. Lond. Ser. A*, 163-98.

Hardy, M. P. (1973). *PhD Thesis.* University of Minnesaota, Minneapolis.

Hubbert, M. K., & Willis, D. G. (1957). Mechanics of Hydraulic Fracturing. *Petrol. Trans. AIME*, 153-68.

Inglis, E. C. (1913). Stresses in a plate due to the presence of cracks and sharp corners. *Trans. Inst. Nav. Archit.*, 219-30.

Ingraffea, A. R. (1977). *PhD Thesis.* University of Colorado.

Irwin, G. R. (1948). Fracture Dynamics. *Fracturing of Metals*.

Irwin, G. R. (1958). Fracture. *Handbuch der Physik*, 551-90.

Jaeger, J. C., & Cook, N. G. (1969). *Fundamentals of Rock Mechanics.* Blackwell Publishing.

Kao, C. S. (2011). *Surface Instability as Damage Evolution in Rock.* Minneapolis: PhD diss. University of Minnesota.

Koiter, W. (1965). Disc. of "Rectangle Tensile Sheet with Symmetric Edge Cracks" by O.L. Bowie. *J. Appl. Mech.*, 237.

Kolosov, G. V. (1909). On the Application of the Theory of Functions of a Complex Variable to a Plane problem in the Mathematical Theory of Elasticity. *PhD. diss.*, Dorpat University.

Krech, W. W., Henderson, F. A., & Hjelmstad, K. E. (1974). *A Standard Rock Suite for Rapid Excavation Research. Report of Investigations 7865.* Washington D.C.: U.S. Bureau of Mines.

Labuz, J. F., & Biolzi, L. (1998). Characteristic stength of quasi-brittle materials. *International Jounral of Solids and Structures*, 4191-203.

Labuz, J. F., & Bridell, J. M. (1993). Reducing Frictional Constraint in Compression Testing through Lubrication. *Int. J. Rock Mech.*, 451-55.

Lin, Q. (2010). *Identification of Rock Fracture by Imaging Techniques.* University of Minnesota, Minneapolis: PhD. diss.

Lin, Q., & Labuz, J. F. (2013). Fracture of sandstone characterized by digital image correlation. *International Journal of Rock Mechanics and Mining Sciences*.

Manning, J. (2012). *Size Effect on Fatigue Crack Growth of Berea Sandstone.* Unversity of Minnesota, Minneapolis: M.S. thesis.

McClintock, F. A., & Argon, A. S. (1966). *Mechanical Behavior of Materials.* Addison-Wesley Publishing Co., Inc.

Muskhelishvili, N. I. (1963). *Some Basic Problems of the Mathematical Theory of Elasticity.* Noordhoff, Groningen: 4th ed.

Newman, J. C. (1969). *Master Thesis.* Virginia Polytechnic Institute.

Newman, J. C. (1971). *An improved method of collocation for the stress analysis of cracked plates with various shaped boundaries.* Langley Reseach Center: NASA Report No. TND-6370.

Orowan, E. (1949). Fracture and Strength of Solids. *Report of Progress in Physics*.

Peters, W. H., & Ranson, W. F. (1982). Digital Imaging Techniques in Experimental Stess Analysis. *Optical Engineering*, 21 (3), 427-31.

Rummel, F. (1987). Fracture Mechanics Approach to Hydraulic Fracture. In B. K. Atkinson, *Fracture Mechanics of Rock* (pp. 228-29). London: Academic Press.

Rummel, F., & Winter, R. B. (1983). *J. Earthquake Prediction Res.*, 2, 33-45.

Schmidt, R. A., & Huddle, C. W. (1976). Effect of Confining Pressure on Fracture Toughness of Indiana Limestone. *Proc. 17th U.S. Symp. on Rock Mech.*

Sutton, M. A., Wolters, W. J., Ranson, W. A., & McNeill, S. R. (1983). Determination of Displacements Using an Improved Digital Image Correlation Method. *Image and Vision Computing*, 1 (3), 133-139.

Yamaguchi, I. (1981). Speckle Displacement and Decorrelation in the Diffraction and Image Fields for Small Object Defromation. *International Journal of Optics*, Vol. 28. Issue 10. 1359-376.